

Article

Insights from Dikes for Multistage Granitic Magmatism in the Huayangchuan Uranium Polymetallic Deposit, Qinling Orogen

Wenyi Wang¹, Shuang Tan^{1,2,3,*}, Jianjun Wan¹ , Xuelian Hu¹, Haoyang Peng¹ and Chengdong Liu¹

¹ State Key Laboratory of Nuclear Resources and Environment, East China University of Technology, Nanchang 330013, China; 15717918658@163.com (W.W.); jianjunwan@ecut.edu.cn (J.W.); 13697170079@163.com (X.H.); phy1029097570@163.com (H.P.); hdliu@ecut.edu.cn (C.L.)

² Changsha Uranium Geology Research Institute, CNNC, Changsha 410007, China

³ Hunan Engineering Technology Research Center for Evaluation and Comprehensive Utilization of Associated Radioactive Mineral Resources, Changsha 410007, China

* Correspondence: 201661010@ecut.edu.cn

Abstract: The Huayangchuan U-polymetallic deposit in the Qinling Orogen is a newly verified carbonatite-hosted deposit on the southern margin of the North China Craton (NCC) in Central China. Granitic magmatism is extensively developed in the Huayangchuan deposit area and is lacking analysis on the reasons for these situations; however, its ages, petrogenesis, and relationship with uranium mineralization are not well constrained. Zircon U–Pb ages for the hornblende-bearing granite porphyry and medium-fine-grained biotite granites in close proximity to carbonatite rocks are 229.8 ± 1.1 and 135.3 ± 0.6 Ma, respectively. High-K calc-alkaline series and weakly peraluminous Triassic hornblende-bearing granite porphyry are slightly enriched in light rare earth elements (LREE) with flat heavy rare earth element (HREE) patterns, enriched in Ba and Sr, and depleted in Nb, Ta, P, and Ti, i.e., geochemical characteristics similar to those of adakite-like rocks. The Early Cretaceous medium-fine-grained biotite granites are characterized by LREE enrichment and flat HREE patterns, which belong to high-K calc-alkaline series, and metaluminous belong to weakly peraluminous I-type granite, with U and large ion lithophile element (LILE) enrichment and high field strength element depletion. The high initial $^{87}\text{Sr}/^{86}\text{Sr}$ ratios and enriched Nd ($\epsilon_{\text{Nd}}(t) = -10.7$ to -9.5 and -19.9 to -18.9 , respectively) and Hf ($\epsilon_{\text{Hf}}(t) = -21.8$ to -13.0 and -30.5 to -19.0 , respectively) isotopes revealed that both granitic rocks from the Huayangchuan deposit mainly originated from lower crustal materials, generated by partial melting of the ancient basement materials of the Taihua Group. Triassic hornblende-bearing granite porphyry is significantly different from the mantle origin of the contemporaneous U-mineralization carbonatite. In combination with tectonic evolution, we argue that the Qinling Orogenic Belt was affected by the subduction of the North Mianlian Ocean during the Late Triassic. The ongoing northward subduction of the Yangtze Craton resulted in crustal thickening, forming large-scale Indosinian carbonatites, U-polymetallic mineralization, and contemporaneous intermediate-acid magmatism. Additionally, due to the tectonic system transformation caused by Paleo-Pacific Plate subduction, intracontinental lithosphere extension and lithospheric thinning occurred along the southern NCC margin in the Early Cretaceous. Intense magma underplating of the post-orogeny created a large number of magmatic rocks. The tremendous heat could have provided a thermal source and dynamic mechanism for the Yanshanian large-scale U-polymetallic mineralization events.

Keywords: granitic magmatism; geochemistry; petrogenesis; Huayangchuan U-polymetallic deposits; Qinling Orogenic Belt



Citation: Wang, W.; Tan, S.; Wan, J.; Hu, X.; Peng, H.; Liu, C. Insights from Dikes for Multistage Granitic Magmatism in the Huayangchuan Uranium Polymetallic Deposit, Qinling Orogen. *Minerals* **2024**, *14*, 261. <https://doi.org/10.3390/min14030261>

Academic Editors: Maria Economou-Eliopoulos, Shuiyuan Yang, Hui Rong, Chunying Guo and Jincheng Luo

Received: 9 January 2024

Revised: 24 February 2024

Accepted: 26 February 2024

Published: 29 February 2024



Copyright: © 2024 by the authors. Licensee MDPI, Basel, Switzerland. This article is an open access article distributed under the terms and conditions of the Creative Commons Attribution (CC BY) license (<https://creativecommons.org/licenses/by/4.0/>).

1. Introduction

Uranium is an important strategic resource and a nuclear energy material in China. With the rapid development of the nuclear power industry in China, uranium has played

a significant role in national defense and economic development [1,2]. The Qinling Orogenic Belt in China has experienced a series of complex tectonic evolutions and large-scale magmatic activities, developed several different types of magmatic rocks, and formed one of the most important uranium–gold–molybdenum rare earth polymetallic mineralized concentration areas in China [3–6]. This includes the Jinduicheng porphyry type molybdenum deposit, Dahu orogenic type gold–molybdenum deposit, and Huanglongpu and the Huayangchuan carbonatite type uranium–molybdenum rare earth polymetallic deposits [3–9]. According to the summary of the episodic magmatic activity in the Qinling Orogenic Belt in Mao et al. [9], six major tectothermal events in this area were postulated: (1) Neoproterozoic Trondhjemite–Tonalite–Granodiorite (TTG) magmatism (2.9–2.5 Ga); (2) Paleoproterozoic A-type granitic magmatism (2.0–1.6 Ga); (3) Neoproterozoic magmatism (1100–800 Ma); (4) Early Paleozoic magmatism (520–380 Ma); (5) Early Mesozoic magmatism (230–190 Ma, mineralization); and (6) Middle–late Mesozoic acidic magmatism (170–80 Ma, mineralization) [9]. The last two magmatic activities are closely related to the polymetallic metallogenic events of the Qinling Orogenic Belt [6–12].

The Huayangchuan carbonatite type uranium–niobium rare earth polymetallic deposit is located in the Xiaoqinling area of the Qinling Orogenic Belt, Shaanxi Province [13–18]. The veined and irregular Indosinian carbonatite dike is the ore-bearing rock of this deposit, most of which intrudes the surrounding rocks along brittle faults [15–17]. Much systematic research on carbonatite rocks in the Huayangchuan deposit has been conducted, acquiring new knowledge of petrogenesis, metallogenic processes, and sources of ore-forming materials [13–18]. However, recent research reveals a certain amount of granitic vein intrusion in the Huayangchuan deposit, with observations of several tectonic–thermal events. In addition, field investigation and metallogenic chronology showed that the multistage mineralization in the Huayangchuan deposit may be related to the granitic intrusion above. Additionally, numerous Mesozoic molybdenum, gold, and copper deposits are found in the surrounding area and are closely related to granite, porphyry, and magmatic hydrotherms [4–9]. Bonnetti et al. (2023) [19] studied the early Middle to Upper Jurassic granitic intrusion in several deposits of the Xiazhuang uranium ore field, an important hydrothermal type uranium ore-concentrated area in China. Furthermore, the whole-rock and mineral geochemistry defined a magmatic–hydrothermal genetic model directly related to the intrusion of early Yanshanian granites in the Nanling belt. Zhong et al. (2023) [20] studied the chronology and petrogenesis of the dikes of the Lujing uranium ore field and found that the Mesozoic dikes provided a favorable oxidation reduction interface and secondary structure fractures for a uranium ore-forming space. However, to our knowledge, only a few studies have been conducted on the granitic dikes around the Huayangchuan deposit, with minimal investigations of the genetic relationship between granitic magmatic activity and U–Nb–REE mineralization [21–26].

Therefore, in this study, we investigated the zircon U–Pb age, Hf isotopes, whole-rock major elements, trace elements, and Sr–Nd isotopes of granitic dike rock from drilling in the Huayangchuan deposit to discuss the diagenetic age, magmatic source area, petrogenesis, dynamic background, and significance for uranium polymetallic mineralization.

2. Regional Geology and Deposit Geology

2.1. Regional Geology

The Qinling Orogenic Belt is an important part of the Central China Orogenic Belt, which can be divided into four tectonic units from north to south by several thrust nappe structures: the Xiaoqinling area, North Qinling, South Qinling, and northern margin of the Yangtze Craton (YZC) (Figure 1a,b) [3–8,23–26]. The Xiaoqinling is on the north side of the Luanchuan fault [6–10,27–31]. The Shangdan Suture is the boundary between the North Qinling Belt and the South Qinling Belt, while the South Qinling Belt is separated from the Yangtze Craton by the nearly east–west Mianlue Suture [8–12,30]. The four blocks of the Qinling Orogenic Belt differ in terms of their rock composition, age, and tectonic evolution, forming relatively independent geological bodies. The strata in the Xiaoqinling

are mainly composed of the ancient crystalline basement of the NCC from the Archean to the Paleoproterozoic, Mesoproterozoic, and Neoproterozoic pyroclastic rocks, meta-sedimentary rock series (like the Xiong'er Group, Gaoshanhe Group, and Guandaokou Group of the Changcheng System, and the Guandaokou Group of the Jixian System), and Paleo-Mesozoic strata [15–18,27–29]. Silurian, Devonian, and Carboniferous strata were missing.

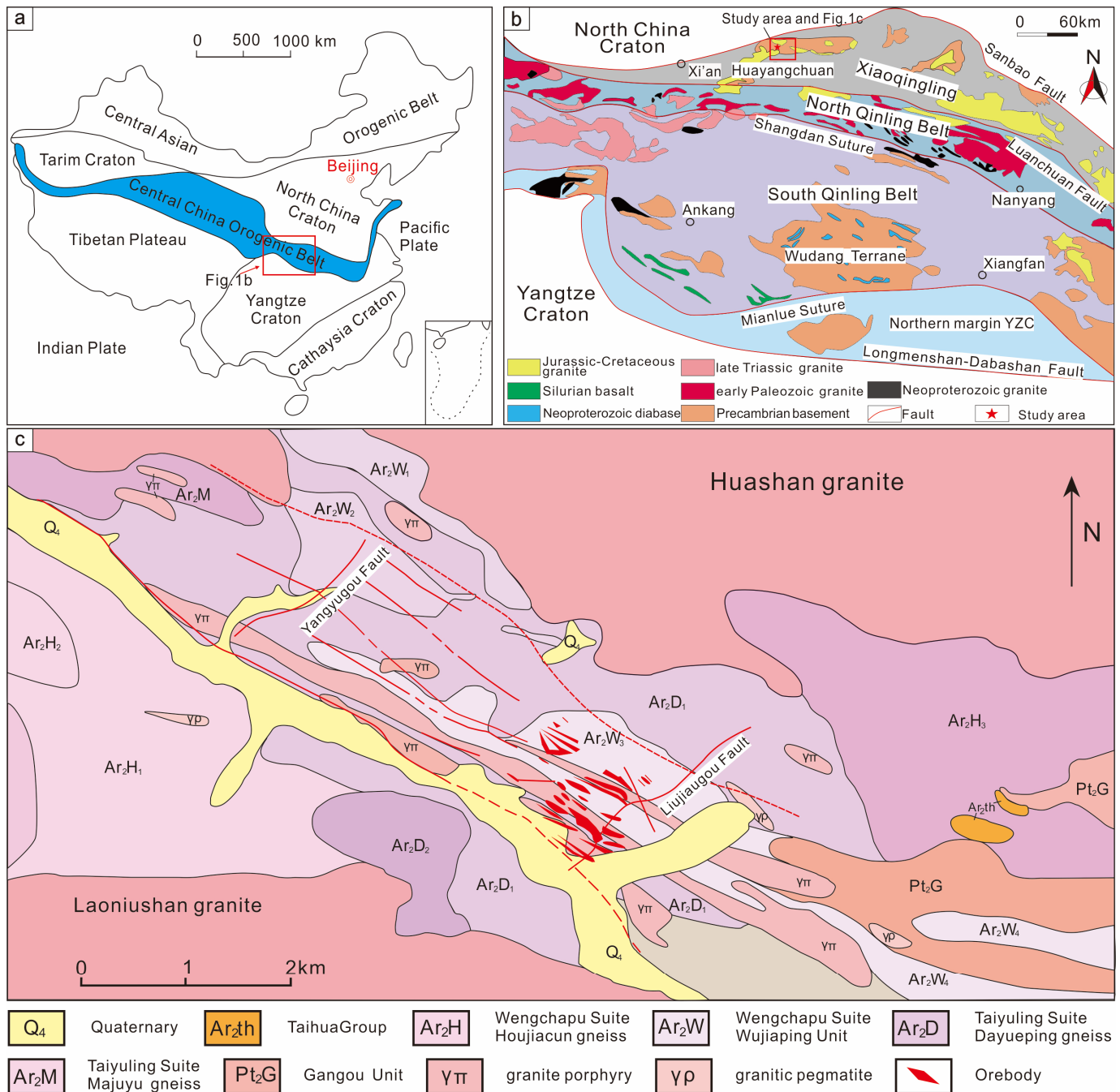


Figure 1. (a) Geological sketch map of China (modified from [28]). (b) Simplified regional tectonic map of the Qinling Orogenic Belt (modified from [3]). (c) Geological map of the Huayangchuan polymetallic deposit (modified from [29]).

The magmatic evolutionary series shows that the Qinling Orogenic Belt has experienced several global orogenic events from the Neoproterozoic to the Cenozoic. The Xiaoqingling

area has also recorded several tectonic–thermal events [3–12,25–31], which could be roughly categorized into three phases: (1) crystalline basement formation of the Neoproterozoic–Paleoproterozoic–Mesoproterozoic; (2) orogeny of the Neoproterozoic–Middle Triassic caused by plate tectonics and crustal accretion; and (3) post-orogenic continental interior tectonic evolution during the Mesozoic–Cenozoic [3–9,25–32]. A large number of pegmatite, granite, granite porphyry, and carbonatite rocks of different ages and petrogeneses have formed in the Xiaoqinling area. With magmatism, large scales of different types of mineralization have formed in this area, relating to magmatic–hydrothermal fluids, including molybdenum, gold, rare earth, uranium, niobium, silver, and lead [6–12,25–33].

As a result of these geological events, a series of structures formed in the Qinling area, especially normal faults and ductile shear zones caused by NW–SE extension in the Early Cretaceous [6–12,34]. The main fault structures in the Xiaoqinling area include the Taiyao, Xiaohe, Huayangchuan, Luonan–Luanchuan, Machaoying, Qinggangping–Jinduicheng, and Zhangjiaping–Bayuan faults. Widely developed faults provide favorable spaces for subsequent magmatism and mineralization [6–12,25–33].

The Mesozoic U, Mo, Au, Ag–Pb–Zn, Cu, W, and rare earth element (REE) mineralization in the Qinling Orogenic Belt can be clearly distinguished into two mineralization stages, corresponding to early and late tectono-magmatic events, respectively [6–12,25–27,29–36]. Early mineralization was closely related to the collision between the NCC and Yangtze Craton in the early Mesozoic, including subduction, collision, and post-orogenic extension processes. The late mineralization stage occurred from the Late Jurassic to Early Cretaceous (ca. 148–114 Ma) and was mainly related to intracontinental extension and lithospheric thinning-destruction of the NCC [6–12,25–27,29–36].

2.2. Deposit Geology

The magmatic activity of the Huayangchuan deposit has been frequent and intense: various magnetites are widely exposed, which can be generally divided into Archean granitic gneisses, Proterozoic granites, Proterozoic pegmatites, Mesozoic granites, Mesozoic carbonatites, basic rocks, and granitic dikes [13–18]. These rocks also record a complex tectonic evolution and multistage episodic magmatism in the Huayangchuan deposit [13–18]. Strong Archean TTG magmatism formed a large area of crystalline granitic gneiss basement in the Xiaoqinling area. Two groups of gneiss suites emerged: the Wengchapu suite ($Ar_{2W}Cgn^1$, before 2.60 Ga, including the Houjiacun unit (Ar_2H) and Wujiaping unit (Ar_2W)) and the Taiyuling suite ($Ar_{2TY}gn^1$, after 2.60 Ga, including the Dayueping unit (Ar_2D) and Majuyu unit (Ar_2M)) (Figure 1c) [13–18].

The main faults of the Huayangchuan deposit are NW oriented, including the Huayangchuan, Taiyao, and Xiaohe faults, whereas the secondary faults and small-scale fractures of the Liujiagou and Yangyugou faults are mostly NE oriented; these faults evolved from Jurassic thrust faults and Cretaceous northern normal faults [13–18]. The ore-bearing carbonatite dikes in the Huayangchuan deposit are controlled by the Huayangchuan fault. The vein groups are NW–NNW oriented, can extend tens of kilometers along the fracture zone, and consist mainly of a large number of small fractures and filled carbonatite dikes. Cai et al. [13] analyzed the fracture stress field in the Huayangchuan deposit based on the attitude of the ore veins, suggesting that the veins may have been the result of NNE–SW extrusion and NWS–SE extrusion tectonic deformation.

With complex geological evolutionary processes, such as the collision of the South China and North China blocks, closure of the Mianlue Ocean, formation of the Qinling Orogenic Belt, and Paleo-Pacific subduction, the Huayangchuan deposit and its surrounding areas experienced strong and extensive Indosinian and Yanshanian magmatic activities and produced a series of Mesozoic granitic plutons, including the Laoniushan complex, Huashan complex, and a large number of intermediate acid dike rocks [4–10,29–36]. The Indosinian lithology is primarily quartz diorite, biotite monzogranite, quartz monzonite, and hornblende-bearing monzonitic granite, whereas the Yanshanian lithology is primarily biotite monzogranite.

The mineralization of uranium, niobium, and REEs in the Huayangchuan deposit is most closely related to carbonatite rocks, which are mostly in the form of irregular network veins, lenses, or dendrites. The mineral resources (e.g., U, Nb, REE, Ba, and Sr; excluding Pb) are mostly associated with or hosted in carbonatite dikes. The mineralization usually presents as dissemination in carbonatites or contact zones between carbonatite dikes and wall rocks. These ore-bearing veins along the brittle fracture intruded the basement rocks of the Archean–Paleoproterozoic Taihua Group, Paleoproterozoic Xiong'er Group, Proterozoic granite pegmatite, and monzonite granite. Carbonatite rocks in the Huayangchuan deposit are widely developed with varying degrees of typical wall rock alteration, including fenitization, silicification, biotitization, chloritization, and actinolitization [13–18]. According to the paragenetic association of the altered minerals, carbonatite veins can be roughly divided into three types: light-colored quartz–calcite veins, aegirine–biotite quartz–calcite ore-bearing veins, and zeolite-bearing quartz–calcite veins. The mineralization zonation at Huayangchuan commonly occurs as veinlets and (locally) stockworks in the carbonatite dykes. Over 40 ore and gangue minerals were identified at Huayangchuan (Figures 2 and 3a). Ore minerals primarily include pyrochlore, allanite, monazite, barite–celestite, galena, minor uraninite, uranothorite, and chevkinite. Major gangue minerals include calcite, aegirine–augite, titanite, apatite, phlogopite, garnet, amphibole, and biotite. Ore-related alteration styles at Huayangchuan primarily include fenitization and potassic alteration. The Mesozoic uranium mineralization in the Huayangchuan deposit is characterized by multistages, including the first-stage uranium metallogenic age of 221.9 ± 5.1 Ma (U-1, uraninite U–Th–Pb EPMA chemical dating) and the second-stage uranium metallogenic age of 133.2 ± 0.96 Ma (U-2, uraninite LA-ICP-MS in situ U–Pb dating), as reported by Huang et al. (2020a,b) [18,29]. Furthermore, the early U-1 mineralization is identified as the product of carbonatite magmatism hydrotherm and the later U-2 mineralization is the result of hydrothermal fluid mobilization and re-mineralization activity [13–18,21,23,26,29]. As mentioned earlier, granitic magmatism is extensively developed in the Huayangchuan deposit area, including granitic pegmatite, granite porphyry, biotite diorite, diorite, lamprophyre, and pyroxenite (Figure 2), but their ages and petrogenesis are not well constrained [13–18,21–24,26,29]. The Mesozoic granitic rocks of the Huayangchuan deposit are mostly in the form of dikes, which are controlled by the Huayangchuan fault zone. They are generally NW trending (280° – 290°) and dip NE, and the dip angles range from 65° to 70° [13–18,21–24,26,29]. In the present study, the granitic dike samples of the borehole were in close contact with ore-bearing carbonatite dikes in space but did not exhibit direct uranium mineralization (Figure 3).

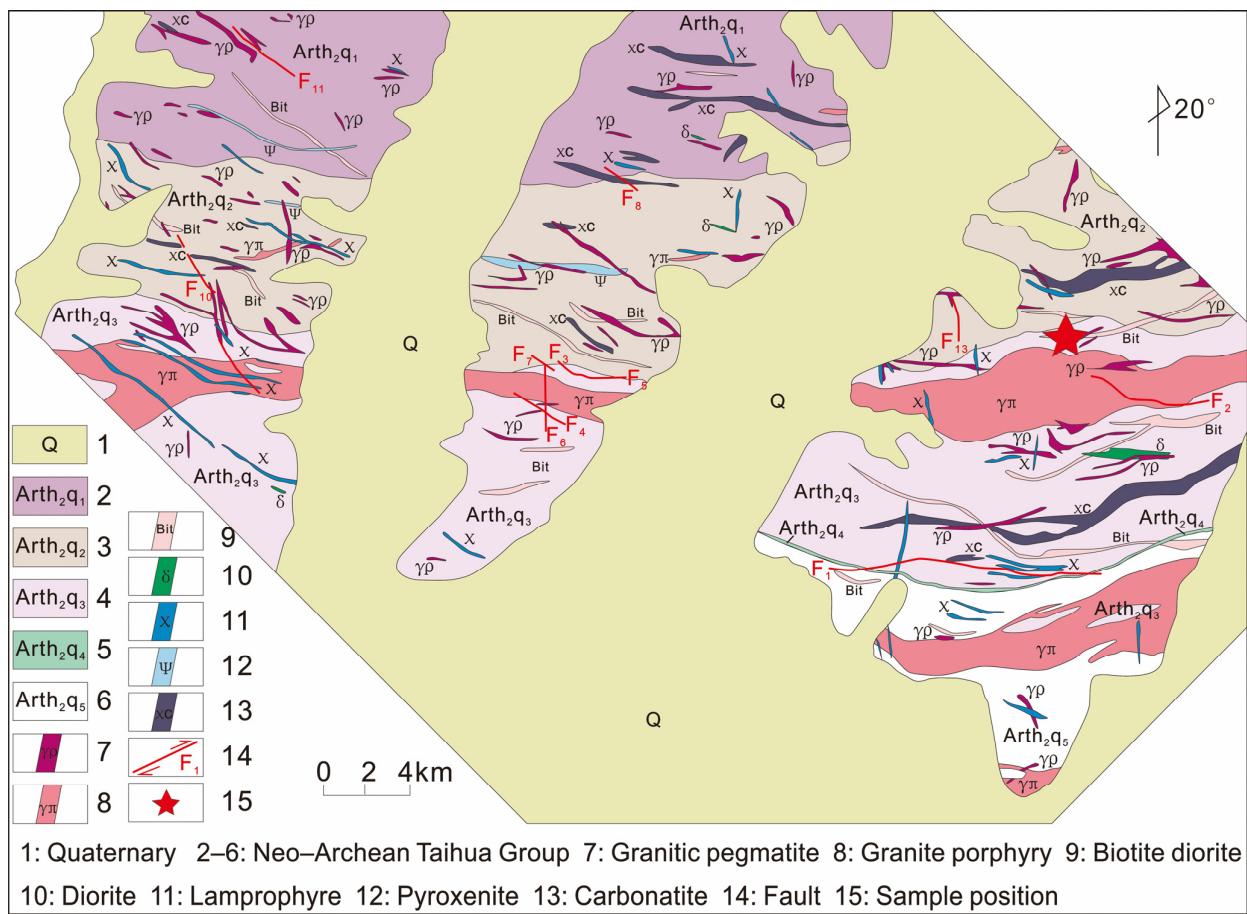


Figure 2. Detailed large-scale geological map of the Huayangchuan deposit (modified after [21,23]).

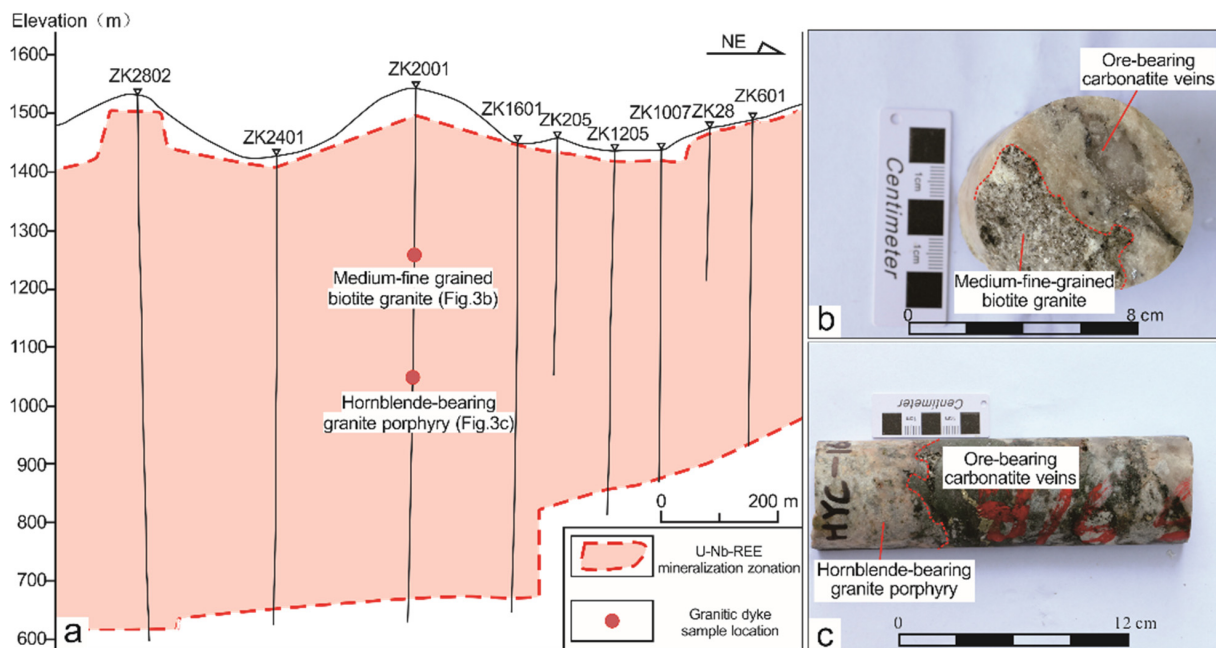


Figure 3. (a) Sampling position diagram for the granitic dikes in the Huayangchuan polymetallic deposit (modified from [17]). (b) Hand specimen photo for the medium-fine-grained biotite granite dikes. (c) Hand specimen photo for the hornblende-bearing granite porphyry dikes.

3. Sampling and Analytical Methods

Granite dikes, which are closely related to ore-bearing carbonatite dikes, were found in the borehole of the Huayangchuan deposit. In the present study, based on detailed geological field investigations of various dikes, two types of granitic rock, hornblende-bearing granite porphyry (19MY01-1–19MY01-4) and medium-fine-grained biotite granite (19MY02-1–19MY02-4) in close proximity to carbonatite rocks, were collected from borehole ZK2001. The specific sampling positions are shown in Figure 3. We then conducted precise LA-ICP-MS zircon U–Pb dating and LA-MC-ICP-MS Hf isotope analysis (Samples 19MY01-1 and 19MY02-2) together with detailed whole-rock major element, trace element, and Sr–Nd isotope analyses.

3.1. Whole-Rock Major and Trace Element Analyses

The whole-rock major and trace elements were analyzed by ALS Chemex (Guangzhou Co., Ltd., Guangzhou, China). Prior to the elemental analyses, the alteration components and surface impurities were cut. The major elements were analyzed via a fluorescence spectrometer (ZSX-100e XRF from Rigak, Tokyo, Japan) with an analysis accuracy of 1%–5%. The detailed analytical procedures are described elsewhere [37]. Trace elements and REEs were analyzed using an X-series 2 inductively coupled plasma mass spectrometry (7900 ICP-MS, Agilen, Santa Clara, CA, USA); the accuracy was typically better than 5%. The detailed analytical procedures are described elsewhere [37].

3.2. Zircon LA-ICP-MS U–Pb Dating and Trace Element Analyses

The zircon grains were separated using conventional heavy liquid and magnetic techniques and handpicked under a binocular microscope. The transmitted light, reflected light, and cathode luminescence (CL) images, as well as the LA-ICP-MS U–Pb isotope and trace element analyses of the zircons, were completed at the State Key Laboratory of Nuclear Resources and Environment, East China University of Technology. Dating and trace elemental analyses were performed using an Agilent 7900 Quadrupole ICP-MS coupled to a GeoLasHD 193 nm laser ablation system. Standard zircon 91,500 and NIST-610 glasses were used for the external calibration of the U–Pb ages and trace element content calculations, respectively [38]. Plešovice zircon was analyzed for every 10 unknown samples for quality control [39]. A laser beam 32 μm in diameter was adopted at a repetition rate of 7 Hz and an energy density of 2.5 J/cm². Offline data processing was performed using the ICP-MS Data Cal program Version 1.0 [40]. Concordia diagrams and weighted mean calculations were performed using Isoplot/Ex_ version 4.15 [40].

3.3. Whole-Rock Sr–Nd Isotope Analyses

The Sr–Nd isotope analysis of the whole rock was performed at Wuhan Sample Solution Analytical Technology Co., Ltd., Wuhan, China. The samples were first dissolved in Teflon bombs with an HF + HNO₃ acid solution for >24 h. The solution was dried, redissolved in HCl, and then separated using the conventional cation exchange technique. Sample preparation and chemical separation were performed as described by Liang et al. [41,42]. The Sr–Nd isotope ratios were measured using a Neptune Plus MC-ICP-MS (Thermo Fisher Scientific, Dreieich, Germany). Mass discrimination correction was performed via internal normalization to an ⁸⁸Sr/⁸⁶Sr ratio of 8.375209 and a ¹⁴⁶Nd/¹⁴⁴Nd ratio of 0.7219. The detailed analytical procedures are described elsewhere [43]. Analyses of the NIST SRM 987 standard solution yielded an ⁸⁷Sr/⁸⁶Sr ratio of 0.710244 ± 22 (2 standard deviations), which is identical within error to published values (0.710241 ± 12) [44]. Analyses of the JNdi-1 standard yielded a ¹⁴³Nd/¹⁴⁴Nd ratio of 0.512118 ± 15 (2 standard deviations), which is identical within error to published values (0.512115 ± 07) [45]. The initial ⁸⁷Sr/⁸⁶Sr ratios and $\epsilon_{\text{Nd}}(t)$ values for the hornblende-bearing granite porphyry and medium-fine-grained biotite granite were calculated based on their respective zircon U–Pb weighted mean ages.

3.4. Zircon LA-MC-ICP-MS Hf Isotope Analyses

The zircon Hf isotopes were analyzed using a Neptune Plus MC-ICP-MS (Thermo Scientific) connected to a RESOLUTION M-50 193 nm laser ablation system at the State Key Laboratory of Isotope Geochemistry, GIGCAS. Detailed descriptions of these two instruments are provided in Zhang et al. [46]. All isotope signals were detected using Faraday cups in static mode. The laser parameters included a 45 μm beam diameter, 6 Hz repetition rate, and 4 J/cm^{-2} energy density. The natural ratio values of $^{176}\text{Yb}/^{173}\text{Yb}$ and $^{176}\text{Lu}/^{175}\text{Lu}$ used in the corrections were 0.79381 [47] and 0.02656 [48], respectively. The mass bias of $^{176}\text{Hf}/^{177}\text{Hf}$ was normalized to $^{179}\text{Hf}/^{177}\text{Hf} = 0.7325$ using an exponential law. A detailed data reduction procedure is reported in Zhang et al. [49].

4. Analytical Results

4.1. Petrography

The hornblende-bearing granite porphyry had a porphyritic and massive structure; the rock-forming minerals were mainly composed of quartz (20%–30%), potassium feldspar (25%–30%), plagioclase (20%–25%), biotite (~10%), and hornblende (~4%). The accessory minerals were zircon, apatite, sphene, and Fe-Ti oxides. The phenocrysts were mainly medium-grained potassium feldspar and quartz (Figure 4a). The hornblende was commonly distributed as an intergranular mineral between feldspar and quartz. The plagioclase in the matrix was partially replaced by sericite with different degrees of argillation, while the biotite was locally altered by chlorite.

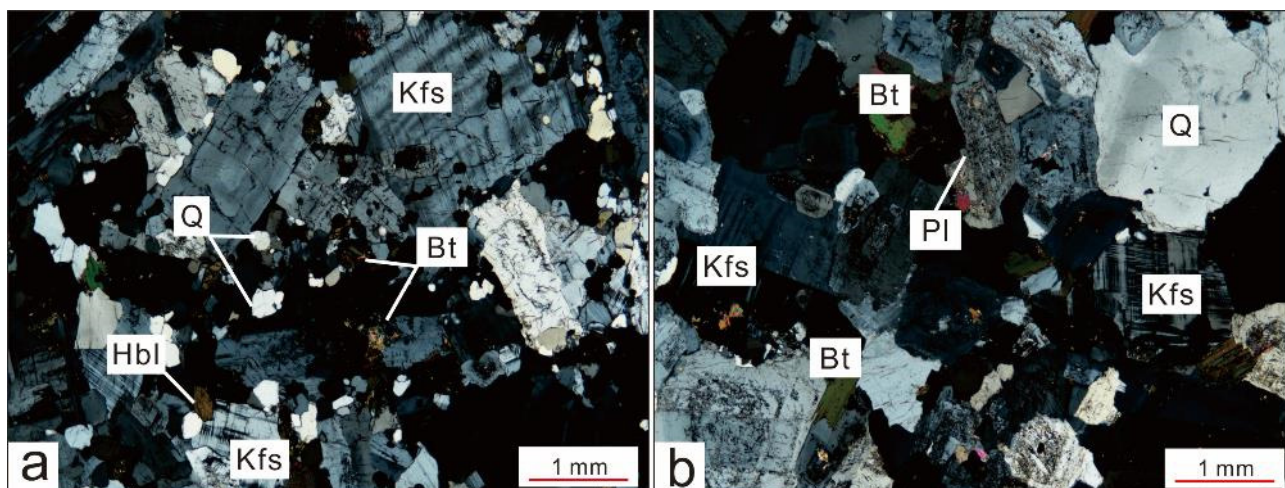


Figure 4. Thin-section photomicrographs of the hornblende-bearing granite porphyry (a) and medium-fine-grained biotite granite (b) (in cross-polarized light). Mineral abbreviations: Bt: biotite; Hbl: hornblende; Kfs: k-feldspar; Pl: plagioclase; and Qtz: quartz.

Medium-fine-grained biotite granite had a typical hypautomorphic granular texture and massive structure. The rock-forming minerals were mainly quartz (25%–30%), potassium feldspar (20%–25%), plagioclase (15%–20%), and biotite (~8%) (Figure 4b). Most potassium feldspars were perthite and plagioclases were oligoclase or andesine. The characteristics of the two feldspars were similar to those of the hornblende-bearing granite porphyry, with different twin crystals and alterations. The mafic minerals were mainly biotite, with a particle size slightly smaller than that of feldspar. K-feldspar was mainly subhedral with cross-hatched twinning, while plagioclase was characterized by polysynthetic twinning and zonation.

4.2. Zircon U–Pb Ages and Trace Elemental Compositions

Representative CL images, U–Pb dating, and trace element data for zircons from samples 19MY01-1 and 19MY02-2 are presented in Table 1 and Figure 5, respectively.

Table 1. Zircon U–Pb isotope and dating data of the hornblende-bearing granite porphyry and medium-fine-grained biotite granite from the Huayangchuan deposit.

Test Spot	Th ($\times 10^{-6}$)	U	Th/U	$^{207}\text{Pb}/^{206}\text{Pb}$		$^{207}\text{Pb}/^{235}\text{U}$		$^{206}\text{Pb}/^{238}\text{U}$		$^{207}\text{Pb}/^{206}\text{Pb}$		$^{207}\text{Pb}/^{235}\text{U}$		$^{206}\text{Pb}/^{238}\text{U}$		Conc.	Use or Not during Weighted Mean Age Calculation	
				Ratio	1 σ	Ratio	1 σ	Ratio	1 σ	Age (Ma)	1 σ	Age (Ma)	1 σ	Age (Ma)	1 σ			
Hornblende-bearing granite porphyry																		
19MY01-1	384	696	0.55	0.05065	0.00121	0.25999	0.00633	0.03739	0.00030	225	92	236	8	238	2	97%	not	
19MY01-2	47.5	138	0.34	0.04854	0.00161	0.24411	0.00764	0.03668	0.00040	129	81	222	7	235	1	96%	use	
19MY01-3	141	274	0.52	0.05528	0.00131	0.27346	0.00643	0.03588	0.00030	408	52	245	4	226	2	99%	use	
19MY01-4	395	1036	0.38	0.05005	0.00121	0.24683	0.00553	0.03588	0.00030	182	49	230	7	226	3	99%	use	
19MY01-5	333	1500	0.22	0.05246	0.00151	0.26944	0.00774	0.03739	0.00040	192	62	241	5	232	4	95%	use	
19MY01-6	106	236	0.45	0.05196	0.00111	0.25728	0.00543	0.03588	0.00030	278	50	230	5	223	2	90%	not	
19MY01-7	64.2	92.3	0.70	0.05146	0.00111	0.25447	0.00563	0.03588	0.00030	148	51	228	4	226	2	97%	use	
19MY01-8	45.7	70.1	0.65	0.05115	0.00211	0.25427	0.10151	0.03628	0.00040	231	89	230	7	235	1	96%	use	
19MY01-9	67.2	77.7	0.86	0.05166	0.00090	0.25547	0.00462	0.03588	0.00030	262	39	231	5	228	3	95%	use	
19MY01-10	125	143	0.87	0.05276	0.00121	0.26120	0.00623	0.03598	0.00030	284	50	234	5	227	2	93%	use	
19MY01-11	37.6	46.3	0.81	0.05206	0.00151	0.26522	0.00764	0.03719	0.00040	345	62	237	3	234	2	98%	use	
19MY01-12	112	147	0.76	0.05357	0.00090	0.26689	0.00513	0.03608	0.00040	308	52	238	11	228	2	96%	use	
19MY01-13	63.1	211	0.30	0.05206	0.00090	0.26562	0.00452	0.03698	0.00020	281	40	237	6	233	1	95%	use	
19MY01-14	151	388	0.39	0.05176	0.00090	0.26673	0.00432	0.03739	0.00030	272	35	238	7	238	2	97%	not	
19MY01-15	255	2460	0.10	0.05095	0.00111	0.25115	0.00513	0.03568	0.00030	231	48	225	5	235	4	90%	use	
Medium-fine-grained biotite granite																		
19MY02-1	891	2540	0.35	0.04992	0.00094	0.14542	0.00287	0.02112	0.00027	191	44	138	3	135	2	97%	use	
19MY02-2	104	204	0.51	0.04656	0.00231	0.13867	0.00662	0.02171	0.00033	33	109	132	6	138	2	95%	use	
19MY02-3	86.9	121	0.72	0.05345	0.00345	0.15194	0.00927	0.02074	0.00037	346	146	144	8	132	2	91%	use	
19MY02-4	130	175	0.74	0.04968	0.00308	0.14197	0.00843	0.02083	0.00032	189	146	135	7	133	2	98%	use	
19MY02-5	72.0	142	0.51	0.04616	0.00367	0.14034	0.01048	0.02183	0.00039	6	181	133	9	139	2	95%	use	
19MY02-6	142	287	0.50	0.04834	0.00187	0.15931	0.00578	0.02399	0.00032	122	95	150	5	153	2	98%	not	
19MY02-7	281	438	0.64	0.05148	0.00191	0.16463	0.00627	0.02307	0.00027	261	85	155	5	147	2	94%	not	
19MY02-8	91.0	191	0.48	0.05207	0.00277	0.16000	0.00800	0.02244	0.00038	287	122	151	7	143	2	94%	not	
19MY02-9	196	301	0.65	0.05216	0.00208	0.16806	0.00717	0.02343	0.00043	300	95	158	6	149	3	94%	not	
19MY02-10	327	1339	0.24	0.05047	0.00122	0.13768	0.00358	0.01972	0.00023	217	53	131	3	126	1	96%	not	
19MY02-11	93.8	197	0.48	0.05138	0.00295	0.15914	0.00923	0.02257	0.00041	257	131	150	8	144	3	95%	not	
19MY02-12	125	210	0.59	0.05103	0.00246	0.15050	0.00698	0.02140	0.00030	243	111	142	6	136	2	95%	use	
19MY02-13	49.9	416	0.12	0.05057	0.00216	0.15386	0.00605	0.02216	0.00029	220	98	145	5	141	2	97%	not	
19MY02-14	93.5	94.3	0.99	0.04749	0.00437	0.13365	0.01143	0.02063	0.00041	72	207	127	10	132	3	96%	use	
19MY02-15	641	1080	0.59	0.04814	0.00174	0.13396	0.00543	0.02016	0.00034	106	87	128	5	129	2	99%	not	
19MY02-16	160	562	0.29	0.04904	0.00187	0.14610	0.00555	0.02158	0.00027	150	89	138	5	138	2	99%	use	
19MY02-17	113	192	0.59	0.05133	0.00406	0.14871	0.01134	0.02121	0.00038	257	183	141	10	135	2	96%	use	
19MY02-18	147	148	0.99	0.05475	0.00364	0.15444	0.00955	0.02078	0.00035	467	144	146	8	133	2	90%	use	
19MY02-19	47.1	48.0	0.98	0.05629	0.00628	0.15728	0.01310	0.02124	0.00074	465	250	148	11	135	5	90%	use	
19MY02-20	63.0	74.3	0.85	0.05503	0.00620	0.15047	0.01369	0.02081	0.00053	413	258	142	12	133	3	93%	use	
19MY02-21	69.4	82.4	0.84	0.04919	0.00526	0.14212	0.01285	0.02164	0.00047	167	224	135	11	138	3	97%	use	
19MY02-22	147	290	0.51	0.04734	0.00269	0.14513	0.00774	0.02237	0.00032	65	130	138	7	143	2	96%	not	
19MY02-23	46.8	57.4	0.82	0.04767	0.00604	0.13569	0.01523	0.01994	0.00058	83	283	129	14	127	4	98%	not	
19MY02-24	133	287	0.46	0.04783	0.00291	0.14083	0.00928	0.02153	0.00044	100	128	134	8	137	3	97%	use	
19MY02-25	128	480	0.27	0.05023	0.00238	0.13624	0.00654	0.01972	0.00029	206	111	130	6	126	2	97%	not	

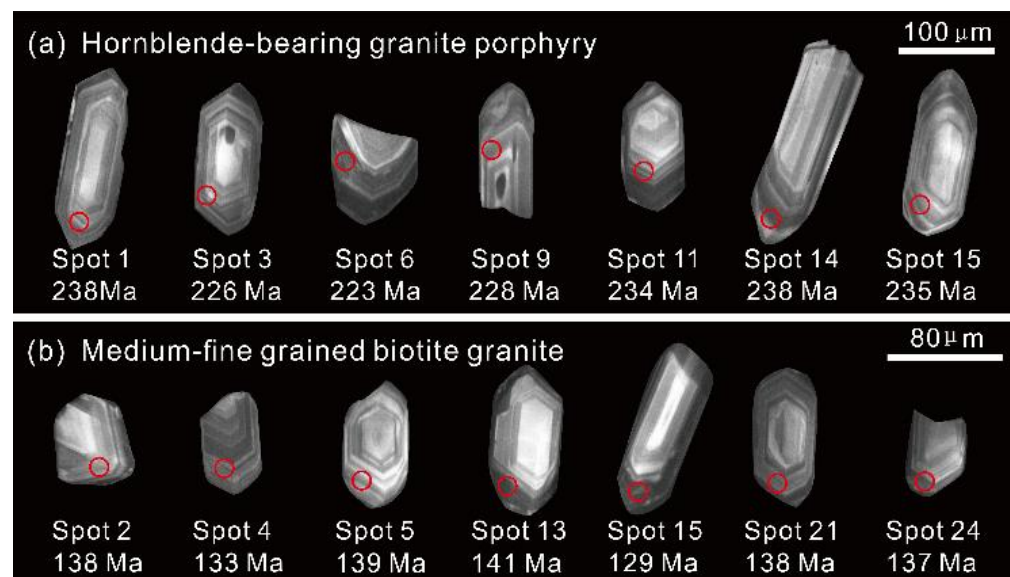


Figure 5. Representative zircon cathode luminescence photographs (CL) and analysis spot age for the hornblende-bearing granite porphyry (a) and medium-fine-grained biotite granite (b). The red circle is the laser ablation analysis spot location of 32 μm ; the lower numbers are the test point number and corresponding age.

4.2.1. Hornblende-Bearing Granite Porphyry

Zircons in the hornblende-bearing granite porphyry (19MY01-1) were mostly idiomorphic, with aspect ratios ranging from 1.5:1 to 4:1 (Figure 5a). Magmatic oscillatory zoning was observed in the CL images of the zircons, with Th/U ratios of 0.10–0.86 and a mean value of 0.53, which is greater than the discriminant value of magmatic zircon, indicating a magmatic origin [44,45]. All zircon test spots were plotted on or near the concordant curve; the concordant $^{206}\text{Pb}/^{238}\text{U}$ apparent age range was 223–238 Ma (Figure 6a). To yield the accurate weighted mean ages with low MSWD values, we selected the zircon test spots and marked them in Table 1. The test positions of the 19MY01-1 and 19MY01-14 zircon spots are located in the joint part of the inner cores and bright rims, and we obtained their mixed $^{206}\text{Pb}/^{238}\text{U}$ ages. In addition, the test spot of 19MY01-6 zircon may suffer the influence of Pb-loss, resulting in a lower concordance of 90%. Therefore, the three test spots above are deleted during the age calculation. The weighted average age of $^{206}\text{Pb}/^{238}\text{U}$ was 229.8 ± 1.1 Ma (MSWD = 3.6, three out of fifteen rejected zircons), which can be regarded as the crystallization age of the hornblende-bearing granite porphyry, indicating that it formed in the Late Triassic and belongs to the Indosinian magmatism.

4.2.2. Medium-Fine-Grained Biotite Granite

Zircons from the medium-fine-grained biotite granite (19MY02-2) were mostly subhedral–anhedral, with lengths of 100–150 μm and length-to-width ratios of 2:1–5:1. They were lighter in color than the hornblende-bearing granite porphyry and showed clear magmatic oscillatory zoning, part of which had a darker core (Figure 5b). The Th/U ratio ranged from 0.12 to 0.99, with a mean value of 0.59, indicating a magmatic origin [50,51]. All zircon test spots were located on or near the concordant curve, and the concordant $^{206}\text{Pb}/^{238}\text{U}$ apparent age range was 126–153 Ma (Figure 6b). To yield the accurate weighted mean ages with low MSWD values, we selected the zircon test spots presented in Table 1. The test positions of the 19MY02-6, 19MY02-7, 19MY02-8, 19MY02-9, 19MY02-11, 19MY02-13, and 19MY02-22 zircon spots are located in the joint part of the inner cores and bright rims, and we obtained their mixed $^{206}\text{Pb}/^{238}\text{U}$ ages. The test spots of 19MY02-10 and 19MY02-25 zircons may suffer the influence of Pb loss. Furthermore, the isotope signal patterns of 19MY02-15 and 19MY02-23 zircon spots showed that the

mineral inclusions were intermixed during the LA-ICP-MS analysis process, resulting in the wrong $^{206}\text{Pb}/^{238}\text{U}$ ages. Therefore, the eleven test spots above were deleted during age calculation. The weighted average age of $^{206}\text{Pb}/^{238}\text{U}$ was 135.3 ± 0.6 Ma (MSWD = 1.6, 11 out of 25 rejected zircons), which can be regarded as the crystallization age of the medium-fine biotite granite. This shows that it formed in the Early Cretaceous and was the product of early Yanshan magmatism.

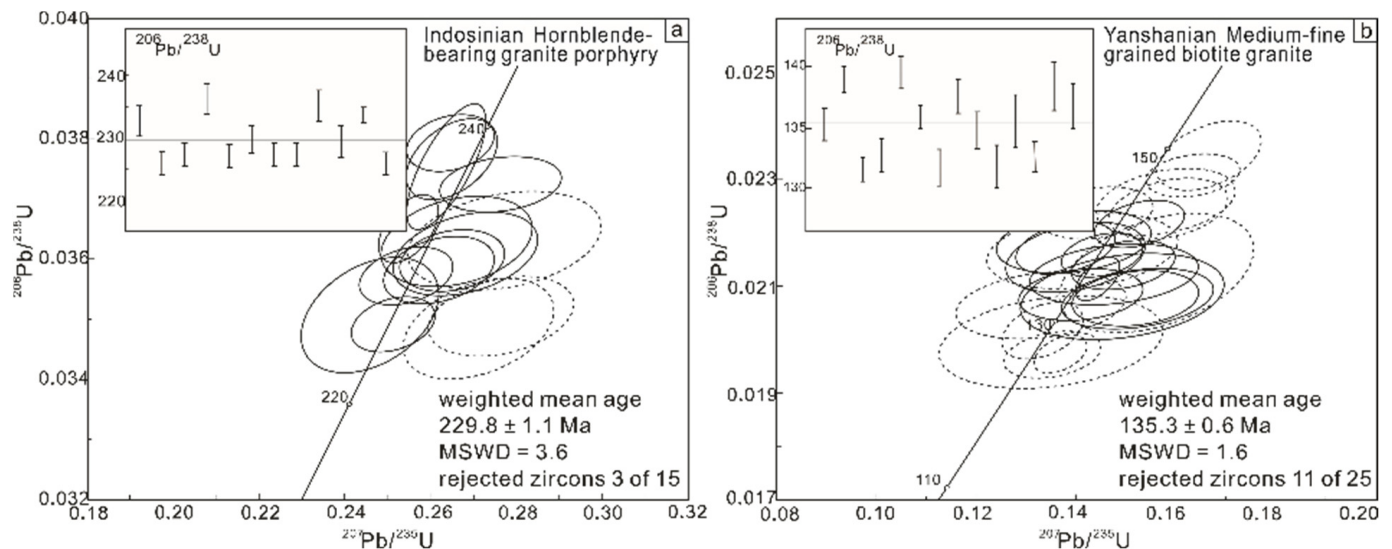


Figure 6. Zircon U–Pb Concordia diagram and weighted mean ages for the hornblende-bearing granite porphyry (a) and medium-fine-grained biotite granite (b). The test spots of solid line circles are usable during weighted mean age calculation. The dotted line circles are eliminated during the weighted mean age calculation.

4.3. Whole-Rock Major and Trace Element Compositions

The major and trace element contents and related geochemical parameters of the two types of granitic rock are listed in Tables 2 and 3. The TAS diagram shows that these samples are all located in the granite scope (Figure 7). The two types of rock were generally silicon rich, with a high ferro–magnesia ratio and relatively low Rittmann Index (mean values of $\sigma = 2.62$ and 2.45 , respectively, both belonging to the calc-alkalic series; Figure 8). The hornblende-bearing granite porphyries had SiO_2 concentrations of 69.21–73.62 wt. % (mean = 70.86 wt. %) and an average $\text{FeO}_T/(\text{FeO}_T + \text{MgO})$ of 0.82. The medium- and fine-grained biotite granites had SiO_2 concentrations of 69.89–71.08 wt. % (mean = 70.46 wt. %) and a mean $\text{FeO}_T/(\text{FeO}_T + \text{MgO})$ of 0.84. In terms of the alkali metal elements, the K_2O and Na_2O contents of the hornblende-bearing granite porphyries were slightly higher than those of the medium-fine-grained biotite granites (mean value of total alkali ($\text{Na}_2\text{O} + \text{K}_2\text{O}$) = 8.53 and 8.20 wt. %, respectively), which indicates that they all belong to the high potassium calc-alkali series. The Na_2O content of the two rock types was slightly higher than the K_2O . The Al_2O_3 content of all samples was similar (mean = 14.89 wt. % and 14.99 wt. %, respectively). The A/CNK ratios of the hornblende-bearing granite porphyries and the medium-fine-grained biotite granites ranged from 0.87 to 1.17 and 0.93 to 1.02, respectively, showing that they all belonged to the metaluminous-weak peralkaline series.

Table 2. Major element compositions (wt. %) and relevant parameters for the hornblende-bearing granite porphyry and medium-fine-grained biotite granite from the Huayangchuan deposit.

No.	19MY01-1	19MY01-2	19MY01-3	19MY01-4	Mean	19MY02-1	19MY02-2	19MY02-3	19MY02-4	Mean
Samples	Hornblende-Bearing Granite Porphyry					Medium-Fine-Grained Biotite Granite				
SiO ₂	70.18	73.62	69.21	70.44	70.86	71.08	70.22	69.89	70.66	70.46
TiO ₂	0.12	0.06	0.17	0.13	0.12	0.22	0.32	0.35	0.26	0.29
Al ₂ O ₃	15.35	15.20	15.15	13.85	14.89	15.12	14.36	15.26	15.22	14.99
Fe ₂ O ₃	2.38	0.95	1.88	2.29	1.88	1.68	2.25	2.62	1.95	2.13
MnO	0.12	0.03	0.10	0.05	0.08	0.05	0.09	0.16	0.09	0.10
MgO	0.49	0.07	0.43	0.68	0.42	0.16	0.44	0.56	0.35	0.38
CaO	2.17	0.38	2.53	2.25	1.83	2.12	2.05	2.01	2.36	2.14
Na ₂ O	4.34	4.35	4.76	4.42	4.47	4.15	4.45	4.28	4.01	4.22
K ₂ O	3.49	4.72	3.78	4.25	4.06	3.90	4.11	3.86	4.05	3.98
P ₂ O ₅	0.14	0.02	0.06	0.05	0.07	0.07	0.10	0.15	0.09	0.10
LOI	0.40	0.36	0.49	0.60	0.46	0.60	0.60	0.45	0.55	0.55
Total	99.18	99.76	98.56	99.01	99.13	99.15	98.99	99.59	99.59	99.33
K ₂ O+Na ₂ O	7.83	9.07	8.54	8.67	8.53	8.05	8.56	8.14	8.06	8.20
K ₂ O/Na ₂ O	0.80	1.09	0.79	0.96	0.91	0.94	0.92	0.90	1.01	0.94
A/CNK	1.03	1.17	0.92	0.87	1.00	1.01	0.93	1.02	1.00	0.99
A/NK	1.40	1.24	1.27	1.17	1.27	1.37	1.22	1.36	1.38	1.33
σ	2.26	2.69	2.78	2.74	2.62	2.31	2.69	2.46	2.35	2.45
A.R.	2.96	3.53	3.33	3.44	3.32	2.86	3.37	2.97	2.68	2.97
Mg [#]	32.42	14.66	34.77	40.90	34.24	18.16	31.31	33.25	29.49	29.37

Note: The formula for A/CNK, A/NK, σ, A.R., and Mg[#] are Al₂O₃/(Na₂O + K₂O + CaO) (molecular ratio), Al₂O₃/(Na₂O + K₂O) (molecular ratio), (Na₂O + K₂O)²/(SiO₂ - 43), (Al₂O₃ + CaO + (Na₂O + K₂O))/((Al₂O₃ + CaO - (Na₂O + K₂O))), and 100 × (MgO/40.31)/(MgO/40.31 + Fe₂O_{3T} × 0.8998/71.85 × 0.85), respectively.

Table 3. Rare earth element and trace element compositions (ppm) and relevant parameters for the hornblende-bearing granite porphyry and medium-fine-grained biotite granite from the Huayangchuan deposit.

No.	19MY01-1	19MY01-2	19MY01-3	19MY01-4	Mean	19MY02-1	19MY02-2	19MY02-3	19MY02-4	Mean
Samples	Hornblende-Bearing Granite Porphyry					Medium-Fine-Grained Biotite Granite				
La	16.8	11.3	13.2	21.6	15.7	36.7	35.6	49.1	30.9	38.0
Ce	33.3	22.4	24.8	38.7	29.8	64.4	55.4	91.1	55.4	66.6
Pr	3.51	1.89	1.96	3.96	2.83	7.18	5.98	10.1	6.31	7.38
Nd	10.4	5.23	5.78	11.8	8.30	27.8	19.7	23.5	19.3	22.6
Sm	2.01	0.91	0.98	2.21	1.53	4.58	2.54	3.51	2.85	3.37
Eu	0.58	0.28	0.33	0.59	0.45	1.21	0.64	0.96	0.79	0.90
Gd	1.67	0.99	1.09	1.71	1.37	3.98	2.10	3.25	2.49	2.96
Tb	0.21	0.15	0.17	0.20	0.18	0.55	0.29	0.42	0.33	0.40
Dy	1.21	0.89	0.92	1.08	1.03	2.89	1.72	2.78	1.42	2.20
Ho	0.22	0.16	0.19	0.21	0.20	0.55	0.41	0.54	0.29	0.45
Er	0.60	0.45	0.54	0.67	0.57	1.32	1.14	1.35	0.75	1.14
Tm	0.09	0.07	0.08	0.10	0.09	0.19	0.12	0.15	0.09	0.14
Yb	0.53	0.41	0.45	0.62	0.50	0.89	0.77	0.92	0.51	0.77
Lu	0.08	0.08	0.07	0.12	0.09	0.13	0.09	0.09	0.09	0.10
Y	2.56	2.41	3.02	6.06	3.51	11.1	12.8	23.9	3.31	12.8
ΣREE	71.2	45.2	50.6	83.5	62.6	152	126	188	121	147
LREE	66.6	42.0	47.1	78.8	58.6	142	120	178	115	139
HREE	4.61	3.20	3.51	4.71	4.01	10.5	6.64	9.50	5.97	8.15
LREE/HREE	14.44	13.13	13.41	16.74	14.43	13.51	18.06	18.76	19.34	17.42
(La/Yb) _N	22.71	19.77	21.10	24.93	22.13	29.56	33.13	38.26	43.40	36.09
δEu	0.97	0.90	0.98	0.93	0.94	0.87	0.85	0.87	0.91	0.87
δCe	1.07	1.19	1.19	1.03	1.12	0.97	0.93	1.00	0.97	0.97
Rb	86.4	54.0	65.6	102	77.0	128	148	245	159	170
Ba	980	615	861	1253	927	1889	958	1860	1682	1597
Th	5.12	6.82	7.84	9.83	7.40	15.4	12.8	9.66	15.1	13.2
U	4.64	9.72	8.28	6.84	7.37	10.3	9.17	15.2	9.07	10.9
Ta	1.15	0.96	1.15	3.65	1.73	1.15	2.98	3.24	2.63	2.50
Nb	21.0	17.7	24.4	23.1	21.5	29.0	39.1	52.4	46.3	41.7
Sr	483	330	450	596	465	870	482	990	944	822
Zr	83.3	54.9	45.1	102	71.4	132	143	252	165	173
Hf	1.79	1.28	1.85	2.16	1.77	2.43	2.26	3.96	3.50	3.04
Cr	4.17	6.78	12.8	5.17	7.23	15.3	4.53	11.5	8.14	9.88
Ni	9.61	7.03	19.3	22.3	14.6	4.18	17.5	36.2	19.2	19.3
V	14.6	45.3	22.4	32.2	28.6	38.9	22.8	41.4	28.6	32.9
Ga	19.1	12.5	8.63	18.8	14.8	22.7	19.2	43.6	29.7	28.8
Pb	21.1	21.3	44.3	55.3	35.5	89.0	53.0	110	77.4	82.4
Sr/Y	188.67	136.93	149.01	98.35	132.48	78.38	37.66	41.42	285.20	64.22
La/Yb	31.70	27.56	29.33	34.84	31.40	41.24	46.23	53.37	60.59	49.35
Nb/Ta	18.26	18.44	21.22	6.33	12.43	25.22	13.12	16.17	17.60	16.68

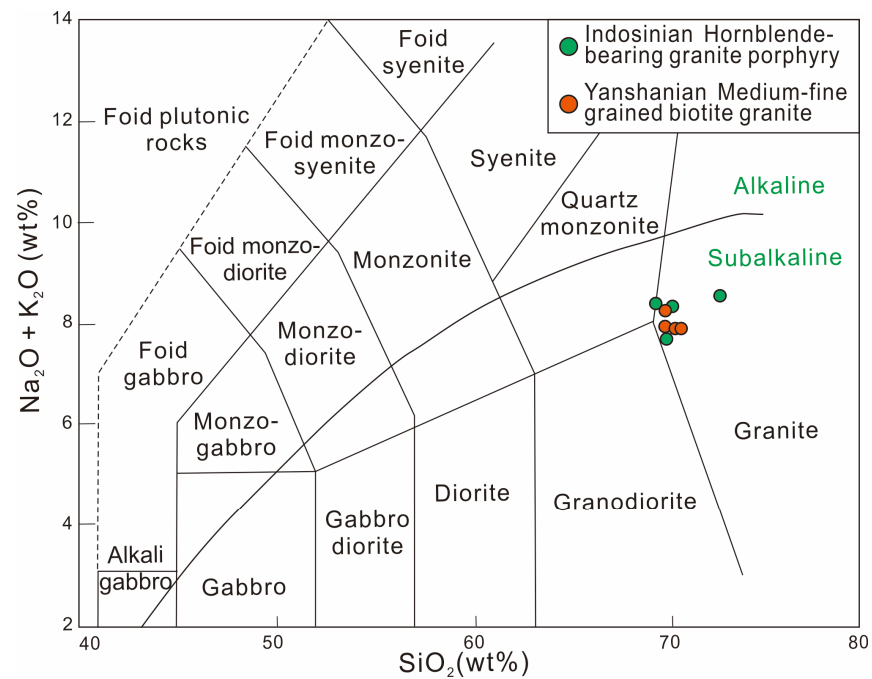


Figure 7. Diagram of SiO₂-K₂O + Na₂O for the granitic dikes in the Huayangchuan deposit (modified from [52]).

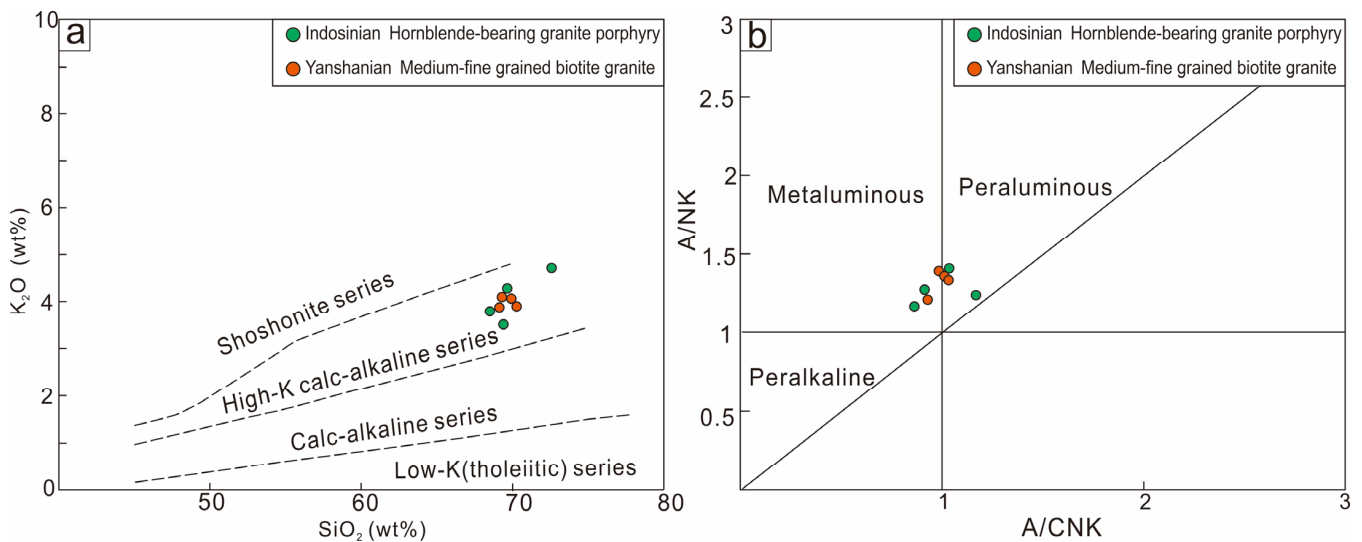


Figure 8. Diagram of SiO₂-K₂O (a) and A/NK-A/CNK (b) for the granitic dikes in the Huayangchuan deposit (modified from [53,54]).

The total REE content of the hornblende-bearing granite porphyry (Σ REE ranged from 45.2 to 83.5 ppm, mean = 62.6 ppm) was lower than that of the medium-fine biotite granite (Σ REE ranged from 121 to 188 ppm, mean = 147 ppm). The average ratio of the HREE/LREE for the two types of samples was 14.43 and 17.42, and the average value of (La/Yb)_N was 22.13 and 36.09, respectively. On the chondrite-normalized REE distribution patterns, both rock types were characterized by strong LREE enrichment relative to the MREE-HREE and weak negative Eu anomalies (mean δ Eu = 0.94 and 0.87, respectively) (Figure 9). The hornblende-bearing granite porphyry and medium-fine-grained biotite granites were rich in the large ion lithophile elements (e.g., Ba and Sr) and LREEs but were relatively deficient in the high field strength elements (e.g., Nb and Ta) and HREEs. These

rocks revealed characteristics similar to those of adakite or high Ba–Sr granites but atypical of I- or S-type granites [25,55–58].

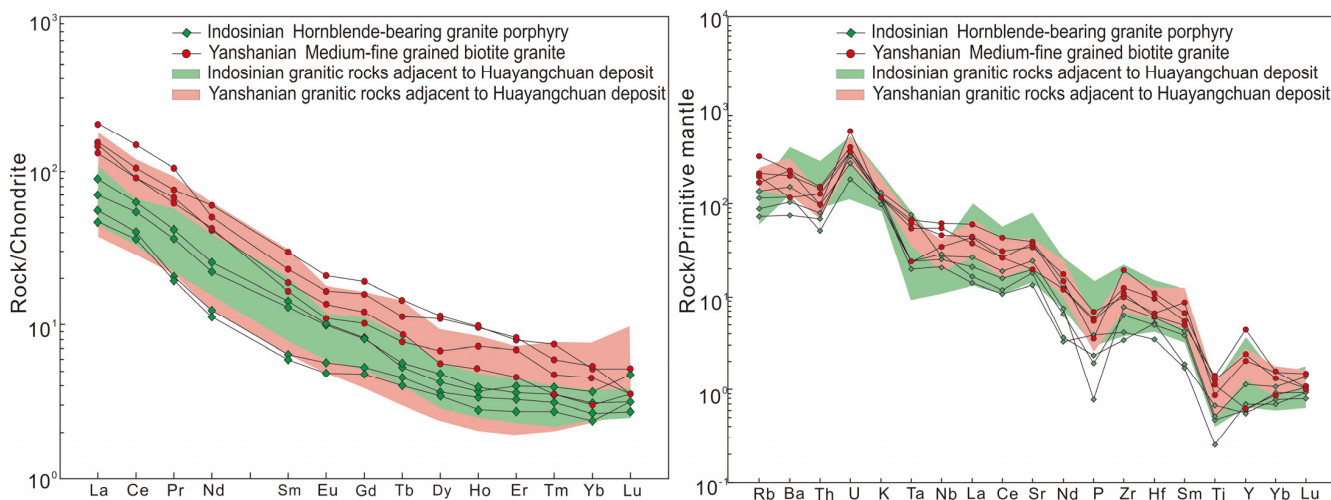


Figure 9. Chondrite-normalized REE distribution pattern and primitive mantle normalized trace element variation diagrams of the granites from the Huayangchuan deposit (normalized values from [55]). Data on Indosinian granitic rocks adjacent to the Huayangchuan deposit were obtained from the Wengyu unit of the Huashan pluton and Laoniushan pluton cited from previous studies [25,35]. Data on Yanshanian granitic rocks were obtained from the Fangshanyu unit of the Huashan pluton, Heyu pluton, Funiushan pluton, Shijiawan pluton, and Laoniushan pluton cited from previous studies [16,25,36,58].

4.4. Whole-Rock Sr–Nd Isotope Composition

The whole-rock Rb–Sr and Sm–Nd isotope data are listed in Table 4 and illustrated in Figure 10. The initial ⁸⁷Sr/⁸⁶Sr ratios and ε_{Nd}(t) values were calculated based on their zircon U–Pb weighted mean ages of 229.8 Ma and 135.3 Ma, respectively. These samples had uniform initial ⁸⁷Sr/⁸⁶Sr ratios of 0.704554–0.704691 and 0.708464–0.708917, ε_{Nd}(t) of –10.7 to –9.5 and –19.9 to –18.9, and two-stage Nd model (T_{DM2}) ages of 1776–1872 and 2462–2535 Ma, respectively.

Table 4. Sr–Nd isotope compositions for the hornblende-bearing granite porphyry and medium-fine-grained biotite granite.

Samples	⁸⁷ Rb/ ⁸⁶ Sr	⁸⁷ Sr/ ⁸⁶ Sr	2σ	(⁸⁷ Sr/ ⁸⁶ Sr) _i	¹⁴⁷ Sm/ ¹⁴⁴ Nd	¹⁴³ Nd/ ¹⁴⁴ Nd	2σ	(¹⁴³ Nd/ ¹⁴⁴ Nd) _i	ε _{Nd} (t)	T _{DM2}
Hornblende-bearing granite porphyry (age = 229.8 Ma)										
19MY01-1	0.517496	0.706254	0.000012	0.704554	0.512017	0.512017	0.000005	0.511840373	–9.8	1797
19MY01-2	0.473391	0.706246	0.000010	0.704691	0.511952	0.511952	0.000006	0.511792989	–10.7	1872
19MY01-4	0.495100	0.706230	0.000012	0.704603	0.512025	0.512025	0.000006	0.511853839	–9.5	1776
Medium-fine-grained biotite granite (age = 135.3 Ma)										
19MY02-2	0.888632	0.710194	0.000012	0.708464	0.511514	0.511514	0.000006	0.511444147	–19.9	2535
19MY02-3	0.716194	0.710015	0.000010	0.708620	0.511572	0.511572	0.000004	0.511491079	–18.9	2462
19MY02-4	0.487437	0.709866	0.000010	0.708917	0.511531	0.511531	0.000006	0.511450997	–19.7	2525

4.5. Zircon Hf Isotope Composition

The zircon Hf isotope compositions are listed in Table 5 and plotted in Figure 11. The samples from the hornblende-bearing granite porphyry had initial ¹⁷⁶Hf/¹⁷⁷Hf ratios and ε_{Hf}(t) values of 0.282032–0.282268 and –21.8 to –13.0, respectively, with corresponding two-stage Hf model ages (T_{DM2}) of 2080–2630 Ma. The samples from the medium-fine-grained biotite granite had initial ¹⁷⁶Hf/¹⁷⁷Hf ratios and ε_{Hf}(t) values of 0.281829–0.282155 and –30.5 to –19.0, respectively, with corresponding two-stage Hf model (T_{DM2}) ages of 2385–3103 Ma.

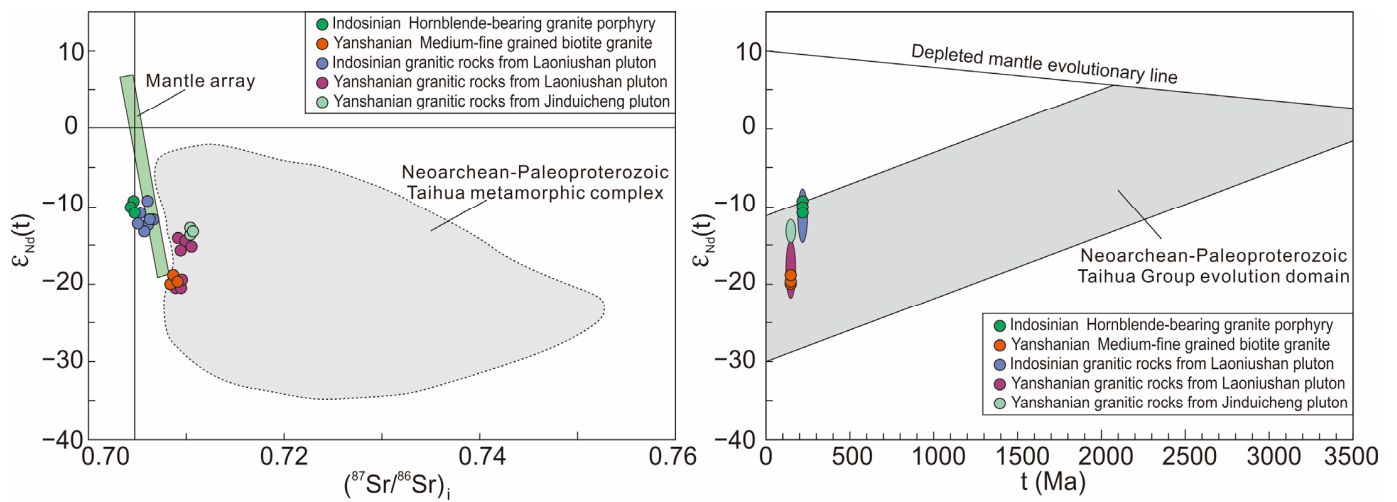


Figure 10. Diagram of the Sr–Nd isotopic correlation for the granites from the Huayangchuan deposit (modified from [59,60]). The data of Indosinian granitic rocks of the Laoniushan pluton are cited in [35]. The data of Yanshanian granitic rocks of the Jinduicheng pluton and Laoniushan pluton are from [16,56].

Table 5. Zircon Hf isotope composition for the hornblende-bearing granite porphyry and medium-fine-grained biotite granite from the Huayangchuan deposit.

Test Spot	$^{176}\text{Lu}/^{177}\text{Hf}$	$^{176}\text{Hf}/^{177}\text{Hf}$	2σ	$(^{176}\text{Hf}/^{177}\text{Hf})_i$	$\epsilon_{\text{Hf}}(0)$	$\epsilon_{\text{Hf}}(t)$	$T_{\text{DM1}}(\text{Ma})$	$T_{\text{DM2}}(\text{Ma})$	$f_{\text{Lu/Hf}}$
Hornblende-bearing granite porphyry									
19MY01–1	0.002890	0.282230	0.000003	0.282218	−19.17	−14.6	1519	2177	−0.9
19MY01–2	0.001764	0.282241	0.000004	0.282233	−18.78	−14.0	1457	2143	−0.9
19MY01–4	0.001649	0.282221	0.000003	0.282214	−19.49	−14.7	1481	2186	−1.0
19MY01–5	0.004613	0.282032	0.000005	0.282012	−26.17	−21.8	1899	2630	−0.9
19MY01–6	0.002059	0.282216	0.000004	0.282207	−19.66	−14.9	1504	2201	−0.9
19MY01–9	0.001489	0.282268	0.000003	0.282262	−17.82	−13.0	1408	2080	−1.0
19MY01–10	0.004901	0.282046	0.000004	0.282025	−25.67	−21.4	1893	2602	−0.9
19MY01–11	0.002986	0.282248	0.000005	0.282235	−18.53	−13.9	1496	2138	−0.9
19MY01–12	0.002649	0.282260	0.000004	0.282249	−18.11	−13.5	1465	2108	−0.9
19MY01–15	0.001686	0.282196	0.000003	0.282189	−20.37	−15.6	1518	2242	−0.9
Medium-fine-grained biotite granite									
19MY02–1	0.001149	0.282081	0.000004	0.282078	−24.44	−21.5	1657	2546	−1.0
19MY02–2	0.001015	0.282066	0.000005	0.282063	−24.97	−22.1	1672	2579	−1.0
19MY02–3	0.001688	0.282139	0.000004	0.282135	−22.39	−19.5	1599	2420	−0.9
19MY02–6	0.000943	0.282062	0.000004	0.282060	−25.11	−22.2	1674	2587	−1.0
19MY02–7	0.001703	0.282155	0.000003	0.282151	−21.82	−19.0	1577	2385	−0.9
19MY02–9	0.001587	0.282102	0.000004	0.282098	−23.69	−20.8	1647	2502	−1.0
19MY02–10	0.001512	0.281905	0.000003	0.281901	−30.66	−27.8	1920	2936	−1.0
19MY02–11	0.001132	0.282065	0.000004	0.282062	−25.00	−22.1	1678	2581	−1.0
19MY02–15	0.001778	0.282019	0.000005	0.282014	−26.63	−23.8	1773	2686	−0.9
19MY02–16	0.001429	0.282152	0.000004	0.282148	−21.93	−19.1	1569	2390	−1.0
19MY02–18	0.001413	0.281829	0.000003	0.281825	−33.35	−30.5	2021	3103	−1.0
19MY02–20	0.001249	0.282021	0.000004	0.282018	−26.56	−23.7	1745	2679	−1.0
19MY02–22	0.001581	0.282103	0.000004	0.282099	−23.66	−20.8	1645	2499	−1.0
19MY02–24	0.001262	0.282026	0.000003	0.282023	−26.38	−23.5	1739	2668	−1.0
19MY02–25	0.002097	0.282059	0.000003	0.282054	−25.21	−22.4	1731	2599	−0.9

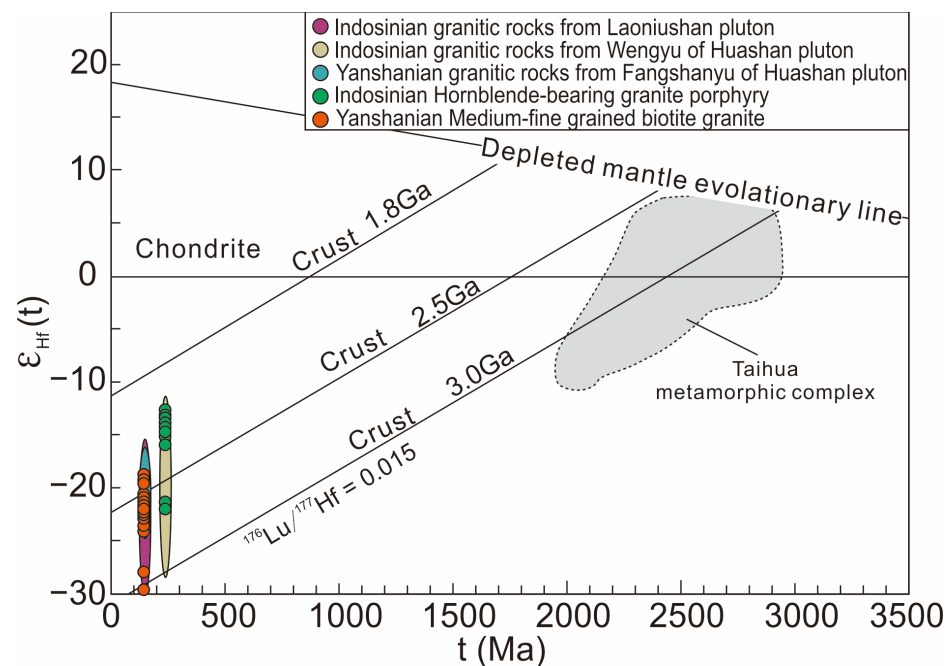


Figure 11. Diagrams of the $\epsilon_{\text{Hf}}(t)$ -ages of zircons in granites from the Huayangchuan deposit (modified from [60–62]). The data of Indosinian granitic rocks of the Laoniushan pluton are cited in [35]. The data of Yanshanian granitic rocks of the Jinduicheng pluton and Laoniushan pluton are from [16,56].

5. Discussion

5.1. Multistage Magmatic Activities

In this study, the age of the hornblende-bearing granite porphyry in close contact with carbonatite rocks in the Huayangchuan deposit was shown to be 229.8 ± 1.1 Ma. The age of the medium-fine biotite granite was 135.3 ± 0.6 Ma. In other words, the products of the strong Mesozoic magmatic activity in the Xiaoqinling and surrounding areas included large-scale veined Indosinian carbonatite, as well as the ~ 230 Ma Indosinian and ~ 130 Ma Yanshanian intermediate-acid magmatic rocks [3–12,25–32,63,64].

Hu et al. [25] obtained the rock-forming ages of the Wengyu and Fangshanyu units in the Huashan complex massif near the Huayangchuan deposit at 205 ± 2 and 132 ± 1 Ma, respectively. Ding et al. [35] also obtained rock-forming ages ranging from 215 to 228 Ma for a series of granitic rocks, such as biotite monzogranite, quartz diorite, quartz monzonite, and hornblende monzonite, from the Laoniushan complex a few kilometers from the southern side of the Huayangchuan deposit. Notably, the rock-forming age result of 229.8 ± 1.1 Ma for the hornblende-bearing granite porphyry in this study is close to the first-stage uranium metallogenic age of 221.9 ± 5.1 Ma in the Mesozoic, which is based on uraninite U–Th–Pb EPMA chemical dating, as reported by Huang et al. [29]. The Early Cretaceous magmatic activity at ~ 130 Ma has also been observed around the Huayangchuan deposit, including the Fangshanyu granite unit of the Huashan Pluton (132 ± 1 Ma) [65], the Laoniushan granitic dike (146 – 152 Ma) [35], monzonitic granites from the Heyu–Wenyu pluton (127 – 138 Ma) [57] and Shijiawan pluton (141.0 ± 0.6 Ma) [58], and granitic porphyry from the Jinduicheng pluton (143.7 Ma) [56]. Furthermore, the age result of 135.3 ± 0.6 Ma for the medium-fine biotite granite in this study is consistent with the second-stage uranium metallogenic age of 133.2 ± 0.96 Ma in the Huayangchuan U-polymetallic deposit, which is based on uraninite LA-ICP-MS in situ U–Pb dating, as obtained by Huang et al. [18]. Therefore, various magmatic rocks of different lithologies and ages are widely exposed near the Huayangchuan deposit. The magmatic activity was frequent and intense in the Xiaoqinling area [6–10,27–32]. Notably, other Mesozoic magmatic rocks exposed near the study area, such as the Jinduicheng porphyry, Shijiawan porphyry, Laoniushan granodior-

ite, and Huashan amphibole-bearing/biotite monzogranite, have the highly similar major, trace, and REE elemental compositions with Huayangchuan granitic rocks. They also display a similar evolutionary trend with Huayangchuan granitic rocks, suggesting that they were probably derived from the partial melting of the same protolith as those of the large contemporaneous magmatic rocks (Figures 9–11) [57–65]. These rocks also record complex tectonic evolution and multistage episodic magmatism in the study area. The large-scale intermediate-acidic magmatic emplacement also led to substantial uranium, REE, and molybdenum polymetallic mineralization; the largest molybdenum metallogenic belt in the Qinling area of China is a typical example [27–30,57–65].

5.2. Granite Petrogenesis

The SiO₂ and K₂O contents of hornblende-bearing granite porphyry were relatively high, while the MgO, TiO₂, Y, and HREE contents were relatively low, indicating that garnet or hornblende may act as a residual mineral in the magmatic source [25,29]. Generally, the partition coefficients of the heavy and medium REEs were high in garnet and hornblende, respectively. The average Y/Yb and (Ho/Yb)_N ratios of the samples in this study were 7.02 and 1.18, respectively, which are close to the discrimination criteria of hornblende residual phase minerals in the magmatic source, with only a small amount of garnet (Figure 12a) [25,29,66–69]. The Late Triassic hornblende-bearing granite porphyry in the Huayangchuan deposit is characterized by a weak negative Eu anomaly (δEu mean value of 0.94), rich Sr (mean value of 465 ppm), rich Ba (mean value of 927 ppm), poor Y (mean value of 3.51 ppm), poor Yb (mean values of 0.50 ppm), high LREE/HREE (mean values of 14.43), high Sr/Y (mean values of 132.48), and high (La/Yb)_N ratios (mean values of 22.13), suggesting that it is similar to high-silica adakites (Figures 12b and 13) [68–72]. In the Sr/Y versus Y and (La/Yb)_N versus Yb_N diagrams, the samples fall within the adakite field (Figures 12b and 13) [66]. Several genetic models have been summarized to account for the origin of adakites and adakitic rocks, including partial melting of a subducted oceanic slab [66,73], partial melting of peridotitic mantle metasomatized by slab melts [68] (Martin et al., 2005), AFC or crystallization fractionation of basaltic magma [74], melting of delaminated mafic lower crust [75], and partial melting of a thickened lower crust [76,77]. The granite porphyries of Huayangchuan have high SiO₂ and K₂O, relatively low MgO (mean values of 0.42) and Mg[#] (mean values of 34), and negative $\epsilon_{\text{Nd}}(t)$ values (mean values of -10.0), which differ from the slab-derived adakites and partial melting of peridotitic mantle metasomatized by slab melts. However, the samples are plotted in the high-K calc-alkaline fields (Figure 8a), a feature that differs distinctly from slab-derived adakites that are sodic. Furthermore, considering the field geological investigation, there is little basalt around the study area. Therefore, the AFC model or crystallization fractionation of basaltic magma can be ruled out. The samples also deviate from the field of adakitic rocks derived from the partial melting of the delaminated lower crust (Figure 14a). In addition, the relatively low values of Mg[#], $\epsilon_{\text{Nd}}(t)$, Cr (mean values of 7.23 ppm), and Ni (mean values of 14.6 ppm) also differ from the product of the partial melting of delaminated mafic lower crust (Mg[#] value and Cr content of adakite formed by the melting of the delaminated mafic lower crust are 53–65 and 200 ppm, respectively) [66–74]. Therefore, based on the adakic characteristics of these rocks combined with the rock assemblage around the study area, we inferred that the Late Triassic hornblende-bearing granite porphyry may have originated from the partial melting of the thickened lower crust, such as the Taihua Group Precambrian crystalline basement in the Qinling region, especially the mafic amphibolites. (Figures 12a and 14a) [6–12,25–32,69–77]. Additionally, the samples had a high La/Yb ratio and relatively slight Ce enrichment, with a mean δCe value of 1.12, which is slightly higher than that of TTG gneiss in the Taihua Group (mean δCe value ≈ 1) [78,79]. Combined with the relatively high Sr and Ba contents, these granite porphyry samples indicate that a certain number of marine sediments may have participated in the partial melting of the ancient basement to form the primary magma (Figure 12a) [25,80].

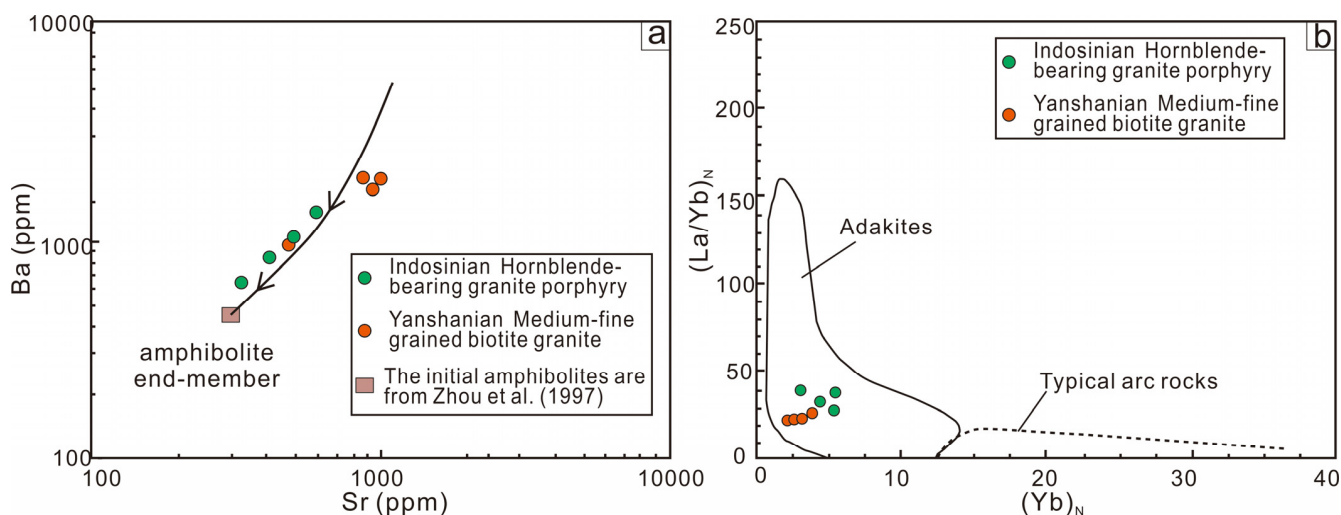


Figure 12. Diagram of Sr vs. Ba (a) and $(La/Yb)_N$ vs. Yb_N (b) for the granites from the Huayangchuan deposit (modified from [66,67]). The curve in (a) shows the calculated trend for the partial melting of the Neoproterozoic to Palaeoproterozoic amphibolites, leaving amphibole + garnet + clinopyroxene as residues. The Sr and Ba values of the initial amphibolites are from [72]. D_{Sr} and D_{Ba} are from [78].

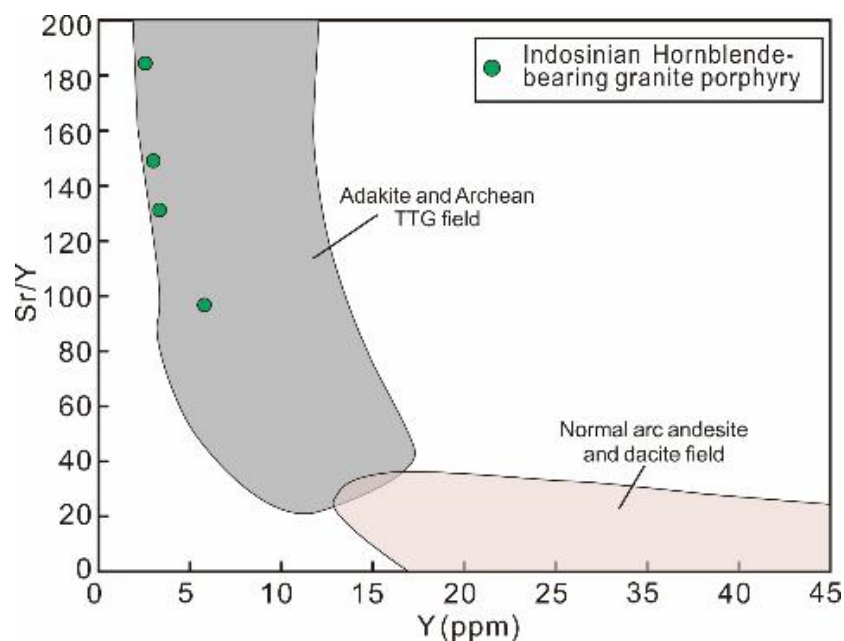


Figure 13. Diagram of Sr/Y vs. Y for the hornblende-bearing granite porphyry from the Huayangchuan deposit (modified from [66]).

The Yanshanian medium-fine-grained biotite granites had a mean Na_2O content of 4.22 wt. % and an A/CNK ratio of 0.99, corresponding to the essential features of highly fractionated I-type granites (Figure 8b) [54,81]. Based on the microphysiography, we found that these samples contain biotite and magnetite, which is inconsistent with A-type granites that typically contain high-temperature anhydrous minerals, or S-type granites that contain Al-enriched minerals. In addition, the reasons for the highly fractionated I-type granites include the relatively high contents of Th and Y (mean values of 13.2 and 12.8 ppm, respectively), the negative correlation between decreasing Na_2O and P_2O_5 and increasing SiO_2 , and the positive correlation between Y and Rb [78,82–87]. The rocks had a negative Eu anomaly (δEu mean value of 0.87) with high Y/Yb and $(Ho/Yb)_N$ ratios (mean values of 16.59 and 1.73, respectively). These characteristics indicate that garnet residue and the frac-

tional crystallization of plagioclase occurred during the evolutionary history of the source magma [69,84]. The Eu anomaly, the depleted Sr and Ba, is associated with the fractional crystallization of plagioclase, potassium feldspar, and apatite [52,54,78–81]. These samples were rich in silicon and low in magnesium and were close to the discrimination criteria for crustal source rocks. The values of Zr/Hf and Y/Yb were higher than the relevant criteria proposed by Eby [85] and Taylor and McLennan [86], indicating that the magmas were the products of the melting of the ancient lower crust (Figures 12 and 14b) [3–12,25–32]. The very low Mg#, Ni, and V concentrations also indicate that little or no mantle material was involved in the origin of the Yanshanian medium-fine-grained biotite granites. Therefore, we suggest that the Yanshanian medium-fine-grained biotite granites in the Huayangchuan deposit were derived from the partial melting of the ancient lower crust, and the magma was controlled by the fractional crystallization of plagioclase, potassium feldspar, apatite, and other minerals. Furthermore, we suggested that the source area of the Yanshanian granites may be relatively deep, which belongs to the unstable area of plagioclase, and there is no plagioclase residue in the source area, so its negative Eu anomaly is not significant.

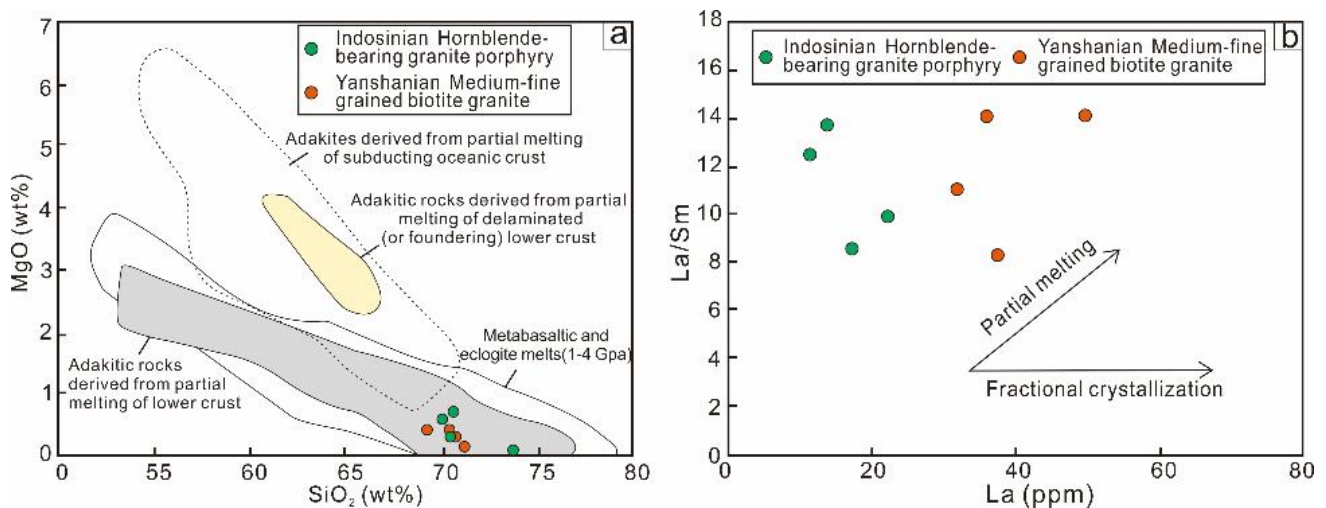


Figure 14. Diagram of MgO vs. SiO₂ (a) and La/Sm vs. La (b) for the granites from the Huayangchuan deposit (modified from [66,88]).

5.3. Implications for Tectonic Evolution and Metallogenesis

Based on the chronology and geochemical characteristics of the magmatic rock in the Xiaoqinling area, our findings show that the study area experienced multiple stages of tectonic–magmatic thermal events during Mesozoic plate subduction and formed large-scale intermediate-acid igneous plutons and U-polymetallic mineralization, with a complex tectonic evolution history [4,27,71]. The Late Triassic and Early Cretaceous granite dikes in the Huayangchuan deposit are representative products of different tectono-magmatic events of the Early and Late Mesozoic in the Xiaoqinling area. Both are located in the post-collision environment shown in the Y + Nb–Rb diagram (Figure 15). Their high-K calc-alkaline characteristics are consistent with granites formed under the tectonic setting of the post-collision orogeny [6–8,12,61].

Combined with the petrogenesis, we inferred that the Indosinian granitic magma emplacement indicates a post-collision extensional environment of the Qinling Orogenic Belt. Records of the subducting plate in the lithospheric mantle under the crust directly indicate Indosinian large-scale polymetallic mineralization in this area [3,6–8,34,57]. The intracontinental extensional environment of the Yanshanian granites agrees with the tectonic regime transition during the Pacific subduction process, which led to large-scale magmatism caused by lithospheric thinning and crustal extension in the Late Mesozoic. The lower crust of the Qinling area may have been influenced by strong basic magma

underplating; the resultant vast amounts of heat may have directly provided the heat source for the ore-forming fluids of the Yanshanian [3,6–8,34,57].

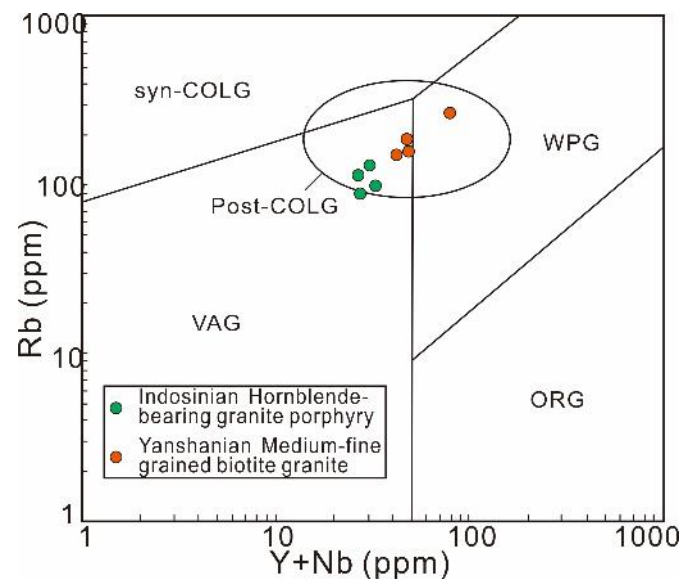


Figure 15. Diagram for tectonic discrimination based on Rb versus (Y + Nb) for the granites from the Huayangchuan deposit (modified from [89]). Syn-COLGs: syn-collision granites; VAGs: volcanic arc granites; WPGs: within-plate granites; ORGs: ocean ridge granites; post-COLGs: post-collision granites.

A series of U-Nb-REE-Mo polymetallic deposits were developed in the Xiaoqingling area. The diagenetic age of hornblende-bearing granite porphyry is approximately same with the mineralogenetic epoch of the Huayangchuan U-polymetallic deposit (221.9 ± 5.1 Ma, uraninite U–Th–Pb [29]), Huanglongpu molybdenum deposit (209–214 Ma, monazite U–Th–Pb) [63], Dashigou molybdenum deposit (228.2 ± 4.7 Ma, molybdenite Re–Os) [58], and Xigou quartz vein type molybdenum deposit (224.6 ± 9.1 Ma, molybdenite Re–Os) [64]. The results suggest that they are all the products of the large-scale Triassic magmatic activities in the Xiaoqingling and surrounding areas. Under the background of post-orogenic intraplate extensional settings, carbonatite magma was formed and intruded into the gneiss of the Taihua Group along the deep fault. The carbonatite dike enriched a large number of radioactive elements (such as U) and formed the uranium polymetallic deposits. In the meantime, the Indosinian granitic rocks were formed in the same geological setting, which may also provide the heat source for uranium mineralization. The diagenetic age of medium-fine-grained biotite granites is in close proximity to the Huayangchuan U-polymetallic deposit (133.2 ± 0.96 Ma, uraninite U–Pb) [18] Jinduicheng porphyry molybdenum deposit (139 ± 3 Ma, molybdenite Re–Os) [56], Xiaoshigou (134 ± 3 Ma, molybdenite Re–Os) [57], and Shijiawan molybdenum deposit (144 ± 1.1 Ma, molybdenite Re–Os) [58]. Therefore, the Yanshanian granitic rocks may have represented the initial extension in the Xiaoqingling area, and this indicates a close genetic relationship between extension-related magmatism and uranium mineralization. Furthermore, based on the fractionated REE patterns and LREE/HREE ratios, Huang et al. (2022) [90] suggested that Yanshanian uranium mineralization may result from the alteration of early uranopyrochlore, indicating that it was precipitated during the high-temperature hydrothermal event that is related to Yanshanian magmatic activity. According to Zheng et al. (2020a, b) [17,26] and Gao et al. (2021) [14], the late-stage uranium mineralization characteristics and mineral paragenesis have also identified this mineralization as the products of the magmatic to high-temperature hydrothermal conditions (different from the precipitation during a magmatic system) due to the Yanshanian magmatic hydrothermal fluid, which leached the uranium element from the early uranium-bearing minerals.

6. Conclusions

Multiple episodes of granitic magmatism have been found in the Huayangchuan polymetallic deposit. Relevant conclusions are as follows.

- (1) Zircon LA-ICP-MS U–Pb dating for the granitic rocks in the Huayangchuan uranium polymetallic deposit redefined two stages of magmatism.
- (2) The hornblende-bearing granite porphyry showed more adakitic affinities. The geochemical features suggest that they were derived from the partial melting of the thickened ancient crust of the Taihua Group.
- (3) The medium-fine-grained biotite granites have I-type granite characteristics and were likely sourced from the partial melting of ancient continental crustal rocks.
- (4) The granite porphyry responded to the late Indosinian tectonic movement of the Qinling area and was broadly coeval with adjacent carbonatite magmas and stage I U mineralization. The biotite granites are typical representatives of magmatic events during the Yanshanian transition of tectonic regimes and provided heat sources for stage II uranium polymetallic mineralization.

Author Contributions: Conceptualization, W.W., S.T. and J.W.; data curation, W.W., X.H. and H.P.; funding acquisition, S.T., J.W. and C.L.; investigation, W.W., S.T. and W.W.; methodology, S.T., J.W. and C.L.; software, S.T.; writing—original draft, W.W., J.W. and X.H.; writing—review and editing, C.L. All authors have read and agreed to the published version of the manuscript.

Funding: This research was funded by the National Natural Science Foundation of China (41772066, 41972043), the scientific research foundation and experimental technology research and development project from the East China University of Technology (DHBK2022007 and DHSY-202250), and the open fund of the Fundamental Science on Radioactive Geology and Exploration Technology Laboratory (RGET2205), Young Talent Program of CNNC and Graduate Student Innovation Fund of Jiangxi Province (YC2023-B208).

Data Availability Statement: The original contributions presented in the study are included in the article.

Acknowledgments: We sincerely appreciate the State Key Laboratory of Isotope Geochemistry, the Guangzhou Institute of Geochemistry, and the Chinese Academy of Sciences (GIGCAS) for helping with zircon Hf analyses and the editors and reviewers for suggestions to improve the manuscript.

Conflicts of Interest: The authors declare no conflicts of interest.

References

1. IAEA. *Geological Classification of Uranium Deposit and Description of Selected Examples*; IAEA Teccod Series; IAEA Teccod 1842; IAEA: Vienna, Austria, 2018.
2. IAEA. *OECD Nuclear Energy Agency Uranium 2018: Resources, Production and Demand (The Red Book)*; IAEA: Vienna, Austria, 2018.
3. Dong, Y.P.; Zhang, G.W.; Hauzenberger, C.; Neubauer, F.; Yang, Z.; Liu, X. Palaeozoic tectonics and evolutionary history of the Qinling orogen: Evidence from geochemistry and geochronology of ophiolite and related volcanic rocks. *Lithos* **2011**, *122*, 39–56. [[CrossRef](#)]
4. Zhang, G.W.; Meng, Q.R.; Yu, Z.P.; Sun, Y.; Zhou, D.W.; Guo, A.L. Orogenesis and dynamics of Qinling orogen. *Sci. China Ser. D* **1996**, *39*, 225–234.
5. Zhai, M.G. Multi-stage crustal growth and cratonization of the North China Craton. *Geosci. Front.* **2014**, *5*, 457–469. [[CrossRef](#)]
6. Chen, Y.J.; Li, N.; Deng, X.H.; Yang, Y.F.; Pirajno, F. *Molybdenum Mineralization in Qinling Orogen*; Science Press: Beijing, China, 2021.
7. Xu, C.; Campbell, I.H.; Allen, C.M.; Huang, Z.L.; Qi, L.; Zhang, H.; Zhang, G.S. Flat rare earth element patterns as an indicator of cumulate processes in the Lesser Qinling carbonatites, China. *Lithos* **2007**, *95*, 267–278. [[CrossRef](#)]
8. Chen, Y.J.; Pirajno, F.; Qi, J.P. The Shangong gold deposit, eastern Qinling Orogen, China: Isotope geochemistry and implications for ore genesis. *Asian J. Earth Sci.* **2008**, *33*, 252–266. [[CrossRef](#)]
9. Mao, J.W.; Pirajno, F.; Xiang, J.F.; Gao, J.J.; Ye, H.S.; Li, Y.F.; Guo, B.J. Mesozoic molybdenum deposits in the east Qinling-Dabie orogenic belt: Characteristics and tectonic settings. *Ore Geol. Rev.* **2011**, *43*, 264–293. [[CrossRef](#)]
10. Deng, X.H.; Chen, Y.J.; Pirajno, F.; Li, N.; Yao, J.M.; Sun, Y.L. The geology and geochronology of the Waifangshan Mo-quartz vein cluster in eastern Qinling, China. *Ore Geol. Rev.* **2017**, *81*, 548–564. [[CrossRef](#)]
11. Ying, Y.C.; Chen, W.; Simonetti, A.; Jiang, S.Y.; Zhao, K.D. Significance of hydrothermal reworking for REE mineralization associated with carbonatite: Constraints from in situ trace element and C-Sr isotope study of calcite and apatite from the Miaoya carbonatite complex (China). *Geochim. Cosmochim. Acta* **2020**, *280*, 340–359. [[CrossRef](#)]

12. Li, N.; Chen, Y.J.; Santosh, M.; Pirajno, F. Compositional polarity of Triassic granitoids in the Qinling Orogen, China: Implication for termination of the northernmost Paleo-Tethys. *Gondwana Res.* **2015**, *27*, 244–257. [[CrossRef](#)]
13. Cai, J.X.; Yu, L.L.; Xu, D.R.; Gao, C.; Chen, G.W.; Yu, D.S.; Jiao, Q.Q.; Ye, T.W.; Zou, S.H.; Li, L.R. Multiple episodes of tectono-thermal disturbances in the Huayangchuan U-Nb-Pb polymetallic deposit in the Xiaoqinling region, central China and their significances on metallogeny. *Ore Geol. Rev.* **2020**, *127*, 103755. [[CrossRef](#)]
14. Gao, L.G.; Chen, Y.W.; Bi, X.W.; Gao, J.F.; Chen, W.T.; Dong, S.H.; Luo, J.C.; Hu, R.Z. Genesis of carbonatite and associated U-Nb-REE mineralization at the Huayangchuan, central China: Insights from mineral paragenesis, chemical and Sr-Nd-C-O isotopic compositions of calcite. *Ore Geol. Rev.* **2021**, *138*, 104310. [[CrossRef](#)]
15. Xue, S.; Ling, M.X.; Liu, Y.L.; Kang, Q.Q.; Huang, R.F.; Zhang, Z.K.; Sun, W.D. The formation of the giant the Huayangchuan U-Nb deposit associated with carbonatite in the Qinling Orogenic Belt. *Ore Geol. Rev.* **2020**, *122*, 103498. [[CrossRef](#)]
16. Yang, C.S.; Zhao, L.D.; Zheng, H.; Wang, D.Q. The multiple granitic magmatism in the giant the Huayangchuan uranium polymetallic ore district: Implications for tectonic evolution of the southern margin of North China Craton in the Qinling Orogen. *Ore Geol. Rev.* **2019**, *112*, 103055. [[CrossRef](#)]
17. Zheng, H.; Chen, H.; Wu, D.; Jiang, H.J.; Gao, C.; Kang, Q.Q.; Yang, C.S.; Wang, D.Q.; Lai, C.K. Genesis of the supergiant Huayangchuan carbonatite-hosted uranium-polymetallic deposit in the Qinling Orogen, Central China. *Gondwana Res.* **2020**, *86*, 250–265. [[CrossRef](#)]
18. Huang, H.; Pan, J.Y.; Zhong, F.J.; Yan, J.; Hong, B.Y.; Kang, Q.Q.; Wan, J.J. LA-ICP-MS in-situ U-Pb dating and genesis of the early cretaceous uraninite in the Huayangchuan U-polymetallic deposit, Shaanxi Province, China. *Acta Mineral. Sin.* **2020**, *40*, 569–583.
19. Bonnetti, C.; Riegler, T.; Liu, X.D.; Cuney, M. Granite-related high-temperature hydrothermal uranium mineralisation: Evidence from the alteration fingerprint associated with an early Yanshanian magmatic event in the Nanling belt, SE China. *Miner. Deposita* **2023**, *58*, 427–460. [[CrossRef](#)]
20. Zhong, F.J.; Xia, F.; Wang, L.; Liu, G.Q.; Pan, J.Y.; Liu, Y.; Li, Z.P. Geochronology and geochemistry of dolerite in the Lujing uranium ore field of central Zhuguangshan complex, and its relationship with uranium mineralization. *Acta Geol. Sin.* **2023**, *97*, 2593–2608. (In Chinese)
21. Hui, X.C.; Li, Z.Y.; Feng, Z.S.; Cheng, D.J. Research on the occurrence state of U in the Huayangchuan U-polymetal deposit, Shanxi Province. *Acta Mineral. Sin.* **2014**, *34*, 573–580. (In Chinese)
22. Li, P.T.; Li, Y.J.; Gu, P.Y.; He, S.P.; Zhuang, Y.J.; Chen, R.M. Paleoproterozoic U-mineralization in Huayangchuan deposit, Xiaoqinling area: Evidence from the U-rich granitic pegmatite. *Minerals* **2023**, *13*, 936. [[CrossRef](#)]
23. Ren, Y.S.; Yang, X.Y.; Wang, G.J. Study on the complex magmatic and hydrothermal metallogenic processes in the giant Huayangchuan uranium (U)-polymetallic ore district: Constraints from geochemical and geochronological evidences. *Ore Geol. Rev.* **2023**, *163*, 105724. [[CrossRef](#)]
24. Meng, Q.F.; Ma, G.Q.; Wang, T.H.; Xiong, S.Q. The Efficient 3D gravity focusing density inversion based on preconditioned JFNK method under undulating terrain: A case study from Huayangchuan, Shaanxi Province, China. *Minerals* **2020**, *10*, 741. [[CrossRef](#)]
25. Hu, J.; Jiang, S.Y.; Zhao, H.X.; Shao, Y.; Zhang, Z.Z.; Xiao, E.; Wang, Y.F.; Dai, B.Z.; Li, H.Y. Geochemistry and petrogenesis of the Huashan granites and their implications for the Mesozoic tectonic settings in the Xiaoqinling gold mineralization belt, NW China. *Asian J. Earth Sci.* **2012**, *56*, 276–289. [[CrossRef](#)]
26. Zheng, H.; Chen, H.Y.; Li, D.F.; Wu, C.; Chen, X.; Lai, C.K. Timing of carbonatite-hosted U-polymetallic mineralization in the supergiant the Huayangchuan deposit, Qinling Orogen: Constraints from titanite U-Pb and molybdenite Re-Os dating. *Geosci. Front.* **2020**, *11*, 1581–1592. [[CrossRef](#)]
27. Dong, Y.P.; Yang, Z.; Liu, X.M.; Sun, S.S.; Li, W.; Cheng, B.; Zhang, F.F.; Zhang, X.N.; He, D.F.; Zhang, G.W. Mesozoic intracontinental orogeny in the Qinling Mountains, central China. *Gondwana Res.* **2016**, *30*, 144–158. [[CrossRef](#)]
28. Zhao, G.C.; Wilde, S.A.; Cawood, P.A.; Sun, M. Archean Blocks and their boundaries in the North China Craton: Lithological, geochemical, structural and P-T path constraints and tectonic evolution. *Precambrian Res.* **2001**, *107*, 45–73. [[CrossRef](#)]
29. Huang, H.; Pan, J.Y.; Hong, B.Y.; Kang, Q.Q.; Zhong, F.J. EPMA chemical U-Th-Pb dating of uraninite in the Huayangchuan U-polymetallic deposit of Shaanxi Province and its geological significance. *Miner. Deposits* **2020**, *39*, 351–368. (In Chinese)
30. Bai, T.; Chen, W.; Jiang, S.Y. Evolution of the carbonatite Mo-HREE deposits in the Lesser Qinling Orogen: Insights from in situ geochemical investigation of calcite and sulfate. *Ore Geol. Rev.* **2019**, *113*, 103069. [[CrossRef](#)]
31. Li, N.; Pirajno, F. Early Mesozoic Mo mineralization in the Qinling Orogen: An overview. *Ore Geol. Rev.* **2017**, *81*, 431–450. [[CrossRef](#)]
32. Liu, J.C.; Wang, Y.T.; Mao, J.W.; Jian, W.; Huang, S.K.; Hu, Q.Q.; Wei, R.; Hao, J.L. Precise ages for lode gold mineralization in the Xiaoqinling goldfield, southern margin of the north China craton: New constraints from in-situ U-Pb dating of hydrothermal monazite and rutile. *Econ. Geol.* **2021**, *116*, 773–786. [[CrossRef](#)]
33. Mao, J.W.; Goldfarb, R.J.; Zhang, Z.W.; Xu, W.Y.; Qiu, Y.M.; Deng, J. Gold deposits in the Xiaoqinling-Xiong'er shan region, Central China. *Miner. Deposita* **2002**, *37*, 306–325. [[CrossRef](#)]
34. Chen, Y.J.; Wang, P.; Li, N.; Yang, Y.F.; Pirajno, F. The collision-type porphyry Mo deposits in Dabie Shan, China. *Ore Geol. Rev.* **2017**, *81*, 405–430. [[CrossRef](#)]
35. Ding, L.X.; Ma, C.Q.; Li, J.W.; Paul, T.R.; Deng, X.D.; Zhang, C.; Xu, W.C. Timing and genesis of the adakitic and shoshonitic intrusions in the Laoniushan complex, southern margin of the North China Craton: Implications for post-collisional magmatism associated with the Qinling Orogen. *Lithos* **2011**, *126*, 212–232. [[CrossRef](#)]

36. Gao, X.Y.; Zhao, T.P.; Chen, W.T. Petrogenesis of the early Cretaceous Funiushan granites on the southern margin of the North China Craton: Implications for the Mesozoic geological evolution. *Asian J. Earth Sci.* **2014**, *94*, 28–44. [[CrossRef](#)]
37. Wiedenbeck, M.; Alle, P.; Corfu, F.; Griffin, W.L.; Meier, M.; Oberli, F.; Von Quadt, A.; Roddick, J.C.; Spiegel, W. Three natural zircon standards for U-Th-Pb, Lu-Hf, trace element and REE analyses. *Geostand. Geoanal. Res.* **1995**, *19*, 1–23. [[CrossRef](#)]
38. Sláma, J.; Košler, J.; Condon, D.J.; Crowley, J.L.; Gerdes, A.; Hanchar, J.M.; Horstwood, M.S.A.; Morris, G.A.; Nasdala, L.; Norberg, N.; et al. Plešovice zircon-A new natural reference material for U-Pb and Hf isotopic microanalysis. *Chem. Geol.* **2008**, *249*, 1–35. [[CrossRef](#)]
39. Liu, Y.S.; Hu, Z.C.; Gao, S.; Günther, D.; Xu, J.; Gao, C.G.; Chen, H.H. In situ analysis of major and trace elements of anhydrous minerals by LA-ICP-MS without applying an internal standard. *Chem. Geol.* **2008**, *257*, 34–43. [[CrossRef](#)]
40. Ludwig, K.R. *User's Manual for Isoplot 3.00: A Geochronological Chronological Toolkit for Microsoft Excel*; Geochronology Center: Berkeley, CA, USA, 2003.
41. Liu, H.Y.; Montaser, A.; Dolan, S.P.; Schwartz, R.S. Evaluation of a low sample consumption, high-efficiency nebulizer for elemental analysis of biological samples using inductively coupled plasma mass spectrometry. *J. Anal. At. Spectrom.* **1996**, *11*, 307–311. [[CrossRef](#)]
42. Liang, X.R.; Wei, G.J.; Li, X.H.; Liu, Y. Precise measurement of $^{143}\text{Nd}/^{144}\text{Nd}$ and Sm/Nd ratios using multiple-collectors inductively couple plasma-mass spectrometer (MC-ICP-MS). *Geochimica* **2003**, *32*, 91–96. (In Chinese)
43. Lin, J.; Liu, Y.S.; Yang, Y.H.; Hu, Z.C. Calibration and correction of LA-ICP-MS and LA-MC-ICP-MS analyses for element contents and isotopic ratios. *Solid Earth Sci.* **2016**, *1*, 5–27. [[CrossRef](#)]
44. Zhang, W.; Hu, Z.C. Estimation of isotopic reference values for pure materials and geological reference materials. *At. Spectrosc.* **2020**, *41*, 93–102. [[CrossRef](#)]
45. Li, C.F.; Li, X.H.; Li, Q.L.; Guo, J.H.; Yang, Y.H. Rapid and precise determination of Sr and Nd isotopic ratios in geological samples from the same filament loading by thermal ionization mass spectrometry employing a single-step separation scheme. *Anal. Chim. Acta* **2012**, *727*, 54–60. [[CrossRef](#)] [[PubMed](#)]
46. Zhang, L.; Ren, Z.Y.; Nichols, A.R.L.; Zhang, Y.H.; Zhang, Y.; Qian, S.P.; Liu, J.Q. Lead isotope analysis of melt inclusions by LA-MC-ICP-MS. *J. Anal. At. Spectrom.* **2014**, *29*, 1393–1405. [[CrossRef](#)]
47. Segal, I.; Halicz, L.; Platzner, I.T. Accurate isotope ratio measurements of ytterbium by multiple collection inductively coupled plasma mass spectrometry applying erbium and hafnium in an improved double external normalization procedure. *J. Anal. At. Spectrom.* **2003**, *18*, 1217–1223. [[CrossRef](#)]
48. Wu, F.Y.; Yang, Y.H.; Xie, L.W.; Yang, J.H.; Xu, P. Hf isotopic compositions of the standard zircons and baddeleyites used in U-Pb geochronology. *Chem. Geol.* **2006**, *234*, 105–126. [[CrossRef](#)]
49. Zhang, L.; Ren, Z.Y.; Xia, X.P.; Li, J.; Zhang, Z.F. IsotopeMaker: A Matlab program for isotopic data reduction. *Int. J. Mass Spectrom.* **2015**, *392*, 118–124. [[CrossRef](#)]
50. Wu, Y.B.; Zheng, Y.F. Tectonic evolution of a composite collision orogen: An overview on the Qinling-Tongbai-Hong'an-Dabie-Sulu orogenic belt in central China. *Gondwana Res.* **2013**, *23*, 1402–1428. [[CrossRef](#)]
51. Hoskin, P.W.O.; Black, L.P. Metamorphic zircon formation by solid-state recrystallization of protolith igneous zircon. *J. Metamorph. Geol.* **2000**, *18*, 423–439. [[CrossRef](#)]
52. Middlemost, E.A.K. Naming materials in the magma/igneous rock system. *Earth Planet. Sci. Lett.* **1994**, *67*, 137–150. [[CrossRef](#)]
53. Peccerillo, A.; Taylor, A.R. Geochemistry of Eocene calc-alkaline volcanic rocks from the Kastamonu area, Northern Turkey. *Contrib. Mineral. Petrol.* **1976**, *58*, 63–81. [[CrossRef](#)]
54. Maniar, P.D.; Piccoli, P.M. Tectonic discrimination of granitoids. *Geol. Soc. Am. Bull.* **1989**, *101*, 635–643. [[CrossRef](#)]
55. McDonough, W.F.; Sun, S.S. The composition of the earth. *Chem. Geol.* **1995**, *120*, 223–253. [[CrossRef](#)]
56. Jiao, J.G.; Tang, Z.L.; Qian, Z.Z.; Yuan, H.C.; Yan, H.Q.; Sun, T.; Xu, G.; Li, X.D. Metallogenic mechanism, magma source and zircon U-Pb age of Jinduicheng granitic porphyry, East Qinling. *J. China Univ. Geosci.* **2010**, *35*, 1011–1022.
57. Mao, J.W.; Xie, G.Q.; Zhang, Z.H.; Li, X.F.; Wang, Y.T.; Zhang, C.Q.; Li, Y.F. Mesozoic large-scale metallogenic pulses in North China and corresponding geodynamic settings. *Acta Petrol. Sin.* **2005**, *21*, 169–188. (In Chinese)
58. Zhao, H.J.; Mao, J.W.; Ye, H.S.; Hou, K.J.; Liang, H.S. Chronology and petrogenesis of Shijiawan granite porphyry in Shannxi Province: Constrains from zircon U-Pb geochronology and Hf isotopic compositions. *Miner. Depos.* **2010**, *29*, 143–157. (In Chinese)
59. Zindler, A.; Hart, S.R. Chemical geodynamics. *Ann. Rev. Earth Planet. Sci. Lett.* **1986**, *14*, 493–571. [[CrossRef](#)]
60. Zhao, H.X.; Jiang, S.Y.; Frimmel, H.E.; Dai, B.Z.; Ma, L. Geochemistry, geochronology and Sr-Nd-Hf isotopes of two Mesozoic granitoids in the Xiaoqinling gold district: Implication for large-scale lithospheric thinning in the North China Craton. *Chem. Geol.* **2012**, *294*, 173–189. [[CrossRef](#)]
61. Hu, H.Z.; Li, N.; Deng, X.H.; Chen, Y.J.; Li, Y. Indosinian Mo mineralization in the Qinling area and prospecting potential. *Geol. China* **2013**, *40*, 549–565. (In Chinese)
62. Deng, X.Q.; Peng, T.P.; Zhao, T.P. Geochronology and geochemistry of the Late Paleoproterozoic aluminous A-type granite in the Xiaoqinling area along the southern margin of the North China Craton: Petrogenesis and tectonic implications. *Precambrian Res.* **2016**, *285*, 127–146. [[CrossRef](#)]
63. Wang, J.Y.; Li, Z.D.; Zhang, Q.; Li, C.; Xie, Y.; Li, G.Y.; Zeng, W.; Ding, N. Metallogenic epoch of the carbonatite-type Mo-U polymetallic deposit in east Qinling: Evidence from the monazite LA-ICP-MS U-Pb and molybdenite ReOs isotopic dating. *Acta Geol. Sin.* **2020**, *94*, 2946–2964.

64. Du, Z.W.; Ye, H.S.; Mao, J.W.; Meng, F.; Cao, J.; Wang, P.; Wei, Z.; Ding, J.H. Molybdenite Re-Os geochronology and isotope geochemical characteristics of Xigou molybdenum deposit in Shaanxi Province and its geological significance. *Miner. Depos.* **2020**, *39*, 728–744. (In Chinese)
65. Zhu, L.M.; Zhang, G.W.; Li, B.; Guo, B. Main geological events, genetic types of metallic deposits and their geodynamical setting in the Qinling Orogenic Belt. *Bull. Mineral. Petrol. Geochem.* **2008**, *27*, 384–390. (In Chinese)
66. Defant, M.J.; Drummond, M.S. Derivation of some modern arc magmas by melting of young subducted lithosphere. *Nature* **1990**, *347*, 662–665. [[CrossRef](#)]
67. Moyen, J.F.; Martin, H.; Jayananda, M. Multi-element geochemical modelling of crust-mantle interactions during late-Archaean crustal growth: The Closepet granite (South India). *Precambrian Res.* **2001**, *112*, 87–105. [[CrossRef](#)]
68. Martin, H.; Smithies, R.H.; Rapp, R.; Moyen, J.F.; Champion, D. An overview of adakite, tonalite-trondhjemite-granodiorite (TTG), and sanukitoid: Relationships and some implications for crustal evolution. *Lithos* **2005**, *79*, 1–24. [[CrossRef](#)]
69. Ge, X.Y.; Li, X.H.; Chen, Z.G.; Li, W.P. Geochemistry and petrogenesis of Jurassic high Sr/low Y granitoids in eastern China: Constrains on crustal thickness. *Chin. Sci. Bull.* **2002**, *47*, 962–968. [[CrossRef](#)]
70. Li, N.; Chen, Y.J.; Zhang, H.; Zhao, T.; Ni, Z. Molybdenum deposits in East Qinling. *Earth Sci. Front.* **2007**, *14*, 186–198.
71. Dong, Y.P.; Santosh, M. Tectonic architecture and multiple orogeny of the Qinling Orogenic Belt, Central China. *Gondwana Res.* **2016**, *29*, 1–40. [[CrossRef](#)]
72. Zhou, H.W.; Li, X.H.; Zhong, Z.Q.; Liu, Y.; Xu, Q.D. Geochemistry of amphibolites within the Taihua complex from the Xiaoqinling area, western Henan and its tectonic implication. *Geochemica* **1997**, *26*, 87–100.
73. Martin, H. Adakitic magmas: Modern analogues of Archaean granitoids. *Lithos* **1999**, *46*, 411–429. [[CrossRef](#)]
74. Castillo, P.R.; Janney, P.E.; Solidum, R.U. Petrology and geochemistry of Camiguin Island, southern Philippines: Insights to the source of adakites and other lavas in a complex arc setting. *Contrib. Mineral. Petrol.* **1999**, *134*, 33–51. [[CrossRef](#)]
75. Gao, S.; Rudnick, R.L.; Yuan, H.L.; Liu, X.M.; Liu, Y.S.; Xu, W.L.; Ling, W.L.; Ayers, J.; Wang, X.C.; Wang, Q.H. Recycling lower continental crust in the North China Craton. *Nature* **2004**, *432*, 892–897. [[CrossRef](#)] [[PubMed](#)]
76. Xu, H.J.; Ma, C.Q.; Ye, K. Early Cretaceous granitoids and their implications for the collapse of the Dabie orogen, eastern China: SHRIMP zircon U–Pb dating and geochemistry. *Chem. Geol.* **2007**, *240*, 238–259. [[CrossRef](#)]
77. Chapman, J.B.; Ducea, M.N.; DeCelles, P.G.; Profeta, L. Tracking changes in crustal thickness during orogenic evolution with Sr/Y: An example from the North American Cordillera. *Geology* **2015**, *43*, 919–922. [[CrossRef](#)]
78. Arth, J.G. Behaviour of trace elements during magmatic processes: A summary of theoretical models and their applications. *J. Res. US Geol. Surv.* **1976**, *4*, 41–47.
79. Diwu, C.R.; Sun, Y.; Lin, C.L.; Liu, X.M.; Wang, H.L. Zircon U–Pb ages and Hf isotopes and their geological significance of Yiyang TTG gneisses from Henan province, China. *Acta Petrol. Sin.* **2007**, *23*, 253–262.
80. Plank, T.; Langmuir, C.H. The chemical composition of subducting sediment and its consequences for the crust and mantle. *Chem. Geol.* **1998**, *145*, 325–394. [[CrossRef](#)]
81. Rickwood, P.C. Boundary lines within petrologic diagrams which use oxides of major and minor elements. *Lithos* **1989**, *22*, 247–263. [[CrossRef](#)]
82. Chappell, B.W.; White, A.J.R. Two contrasting granite types: 25 years later. *Aust. J. Earth Sci.* **2001**, *48*, 489–499. [[CrossRef](#)]
83. Chappell, B.W. Aluminium saturation in I- and S-type granites and the characterization of fractionated haplogranites. *Lithos* **1999**, *46*, 535–551. [[CrossRef](#)]
84. Clemens, J.D. S-type granitic magmas-petrogenetic issues, models and evidence. *Earth-Sci. Rev.* **2003**, *61*, 1–18. [[CrossRef](#)]
85. Eby, G.N. Chemical subdivision of the A-type granitoids: Petrogenetic and tectonic implications. *Geology* **1992**, *20*, 641–644. [[CrossRef](#)]
86. Taylor, S.R.; McLennan, S.M. The Continental crust: Its composition and evolution. *J. Geol.* **1985**, *94*, 196–197.
87. Green, T.H. Significance of Nb/Ta as an indicator of geochemical processes in the crust-mantle system. *Chem. Geol.* **1995**, *120*, 347–359. [[CrossRef](#)]
88. Rapp, R.P.; Watson, E.B.; Miller, C.F. Partial melting of amphibolite/eclogite and the origin of Archean trondhjemites and tonalites. *Precambrian Res.* **1991**, *51*, 1–25. [[CrossRef](#)]
89. Pearce, J.A.; Harris, N.B.W.; Tindle, A.G. Trace element discrimination diagrams for the tectonic interpretation of granitic rocks. *J. Petrol.* **1984**, *25*, 956–983. [[CrossRef](#)]
90. Huang, H.; Wang, K.X.; Cuney, M.; Pan, J.Y.; Bonnetti, C.; Liu, X.D.; Zhong, F.J. Mesozoic magmatic and hydrothermal uranium mineralization in the Huayangchuan carbonatite-hosted U-Nb-polymetallic deposit, North Qinling Orogen (Central China): Evidence from uraninite chemical and isotopic compositions. *Ore Geol. Rev.* **2022**, *146*, 104958. [[CrossRef](#)]

Disclaimer/Publisher’s Note: The statements, opinions and data contained in all publications are solely those of the individual author(s) and contributor(s) and not of MDPI and/or the editor(s). MDPI and/or the editor(s) disclaim responsibility for any injury to people or property resulting from any ideas, methods, instructions or products referred to in the content.